
CENTRO BRASILEIRO DE PESQUISAS FÍSICAS
http://www.cbpf.br

MICROSCOPIA ELETRÔNICA

ANDRÉ LUIZ PINTO

CBPF

Roteiro

- Introdução
- Fundamentos
  - Fontes de elétrons
  - Lentes de elétrons
  - Interação elétron-matéria
- Microscópio Eletrônico de Varredura
- Microscópio Eletrônico de Transmissão
- Aplicações à Nanotecnologia
- Comentários Finais
  - LabNano

Opções para visualizar a microestrutura

- Aumento x Resolução (lateral)

- Olho humano – 0,1 mm
- Microscopia Ótica – 0,5 μm
- Microscópio Eletrônico de Varredura (MEV) – 1 - 4 ηm
- Microscópio Eletrônico de Transmissão (MET) – 0,8 - 1,4 Å
- Microscópio de Ponta de Prova (SPM) – 0,3 Å

Revestimento nc-TiC/a-C

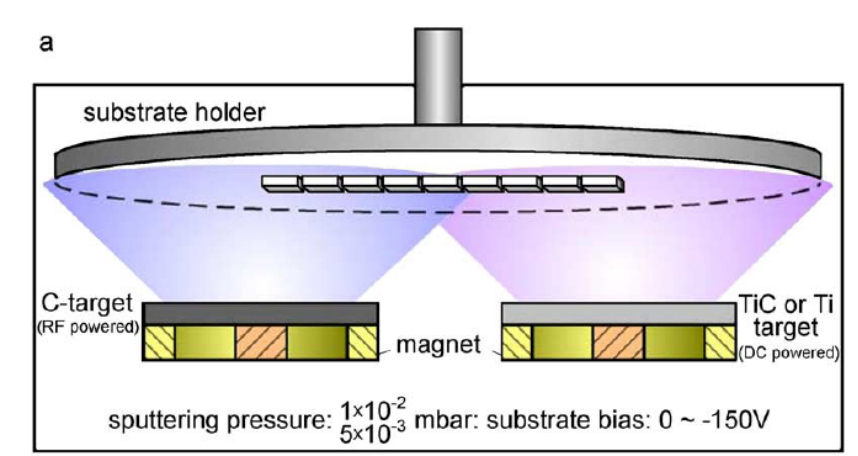

Pei et al. (2005)

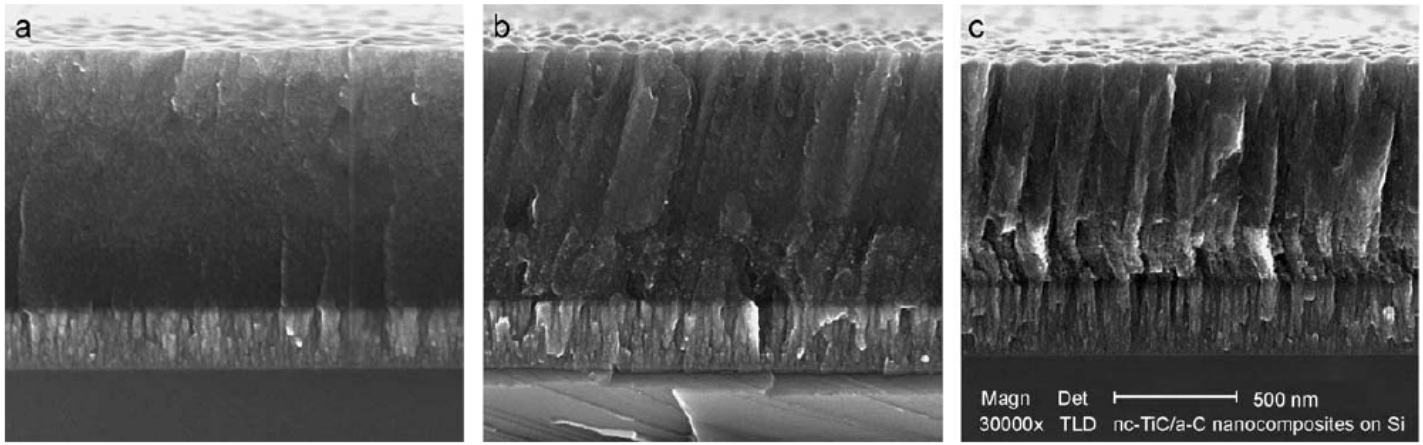

Fig. 2. SEM micrographs of the fractured cross-sections showing the transition from glassy to columnar growth of nc-TiC/a-C coatings with Ti content (at.%) of (a) 10, (b) 17 and (c) 34.

Revestimento nc-TiC/a-C

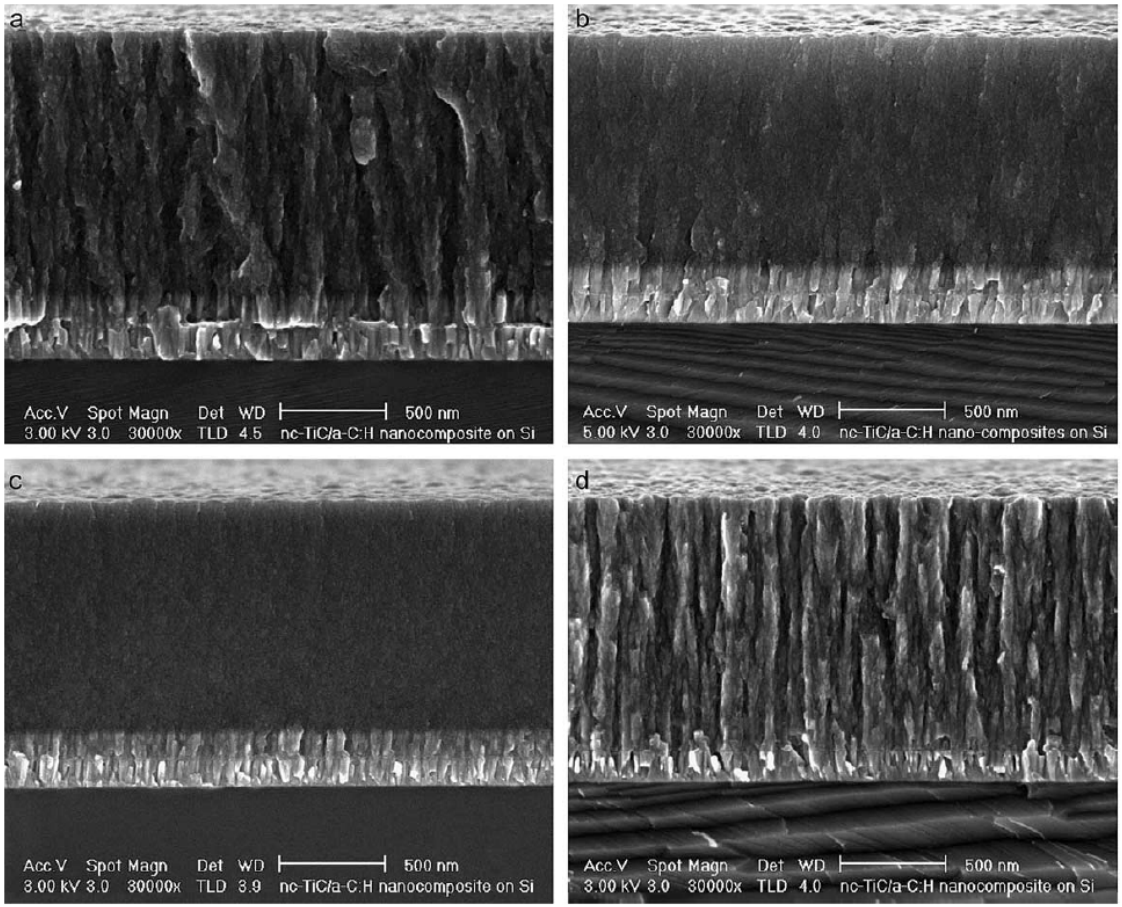

Fig. 3. SEM micrographs of fractured cross-sections showing the transition from columnar to glassy structures of nc-TiC/a-C:H coatings deposited under different conditions: (a) 110 sccm C_2H_2 and −60 V bias; (b) 110 sccm C_2H_2 and −100 V bias; (c) 110 sccm C_2H_2 and −150 V bias and (d) 80 sccm C_2H_2 and −100 V bias.

Pei et al. (2005)

Revestimento nc-TiC/a-C

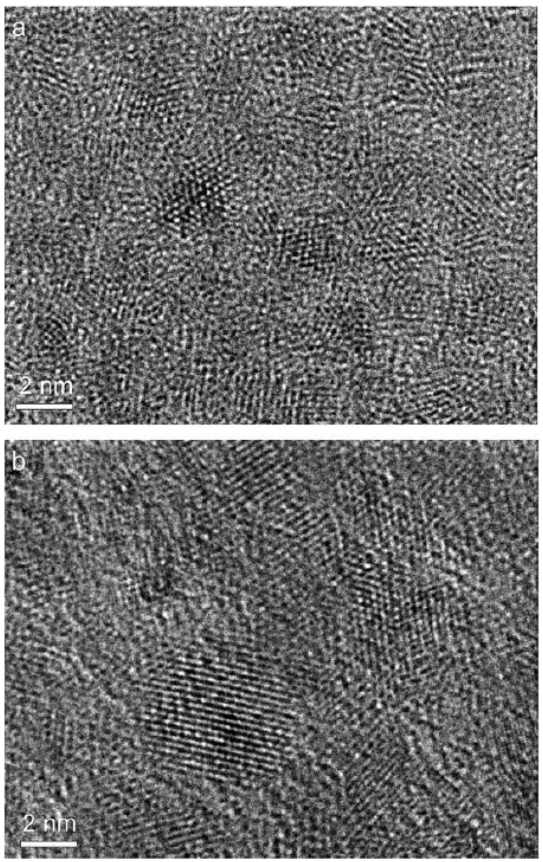

Fig. 4. HRTEM micrographs showing TiC nanocrystallites embedded in a-C:H matrix in nc-TiC/a-C:H nanocomposite: (a) coating HB3 with 17.84 at.% Ti and (b) coating HB5 with 31.75 at.% Ti.

Pei et al. (2005)

Nanoestruturação de superfícies

Nano region width = 22 μm;
Micron region width = 40 μm

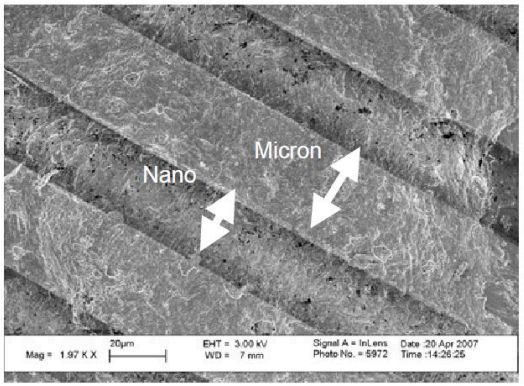

(g) Patterned Ti substrates
(scale bar = 20 μm)

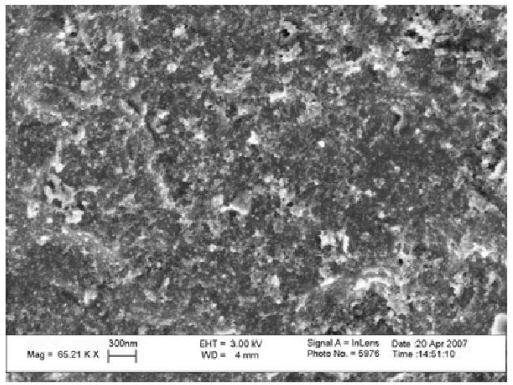

(h) Micron region on patterned Ti substrate
(scale bar = 300 nm)

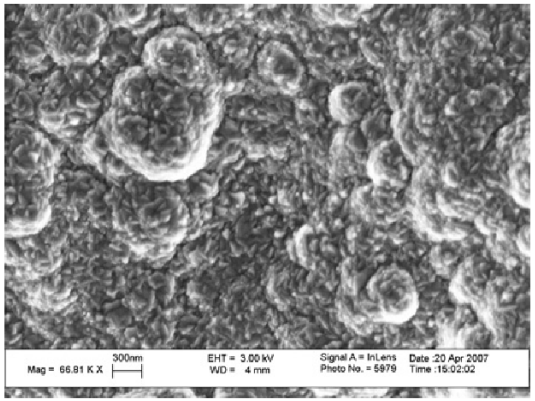

(i) Nano region on patterned Ti substrate
(scale bar = 300 nm)

Pucket et al. 2008

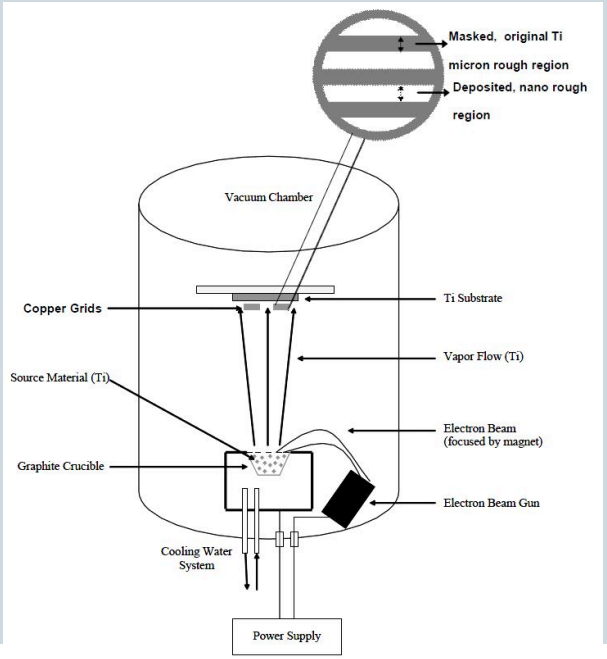

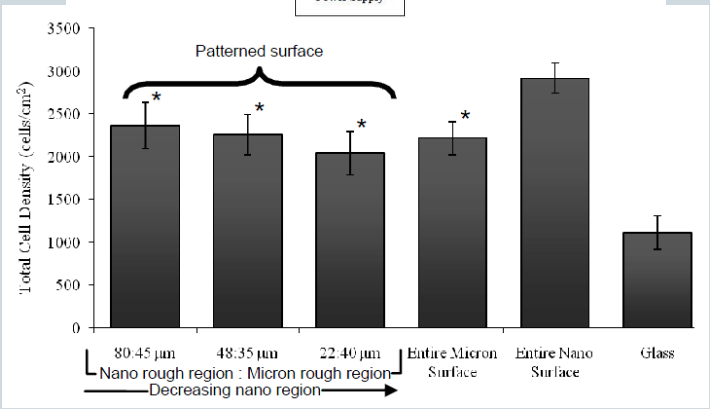

Sensitividade a modificações superficiais de biomateriais

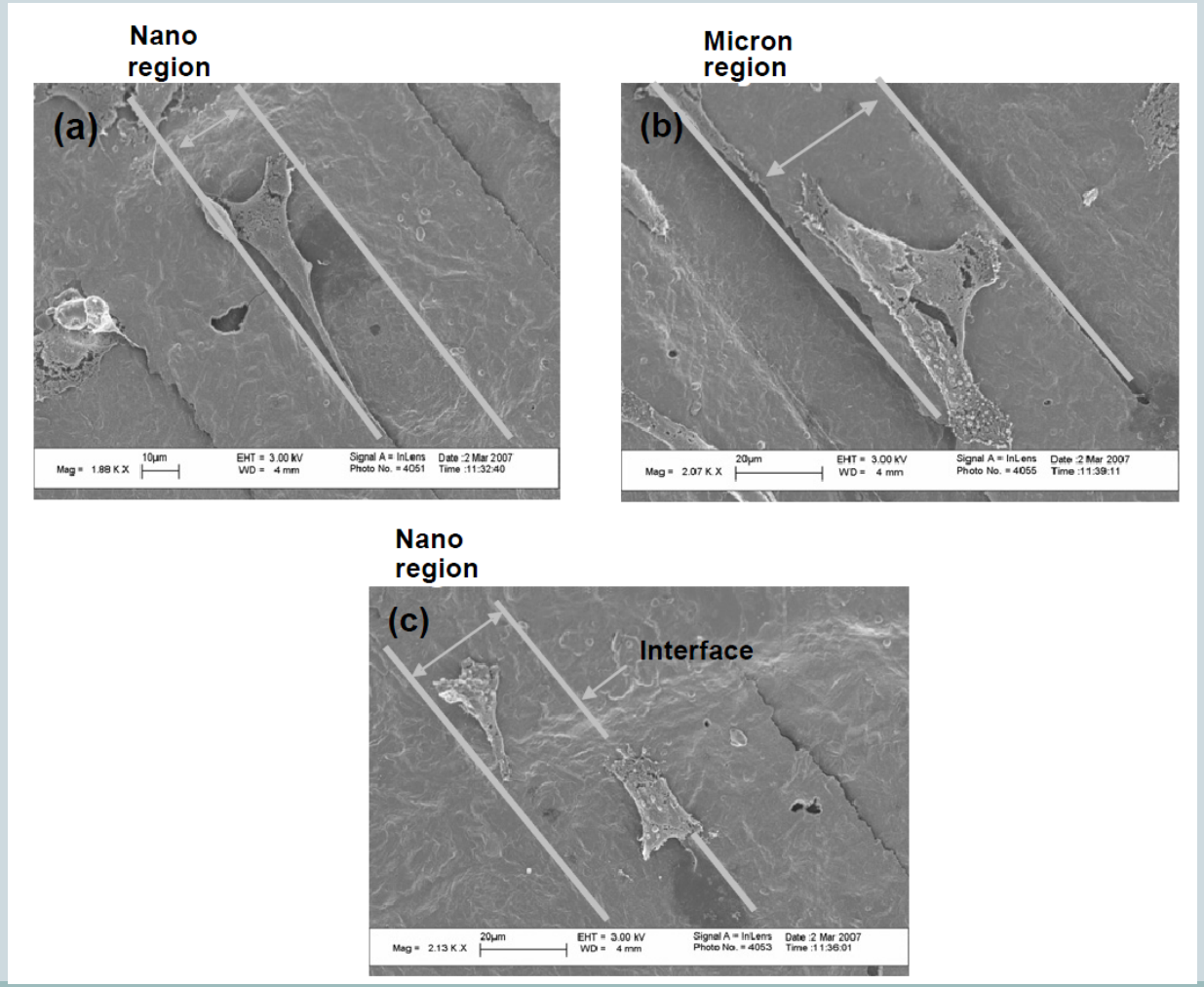

Pucket et al. 2008

Sensitividade a modificações superficiais de biomateriais

- Nanolitografia por Feixe de Elétrons para modificação superficial visando aumento da biocompatibilidade.
- Limite de sensibilidade por fibroblastos ~ 35 nm

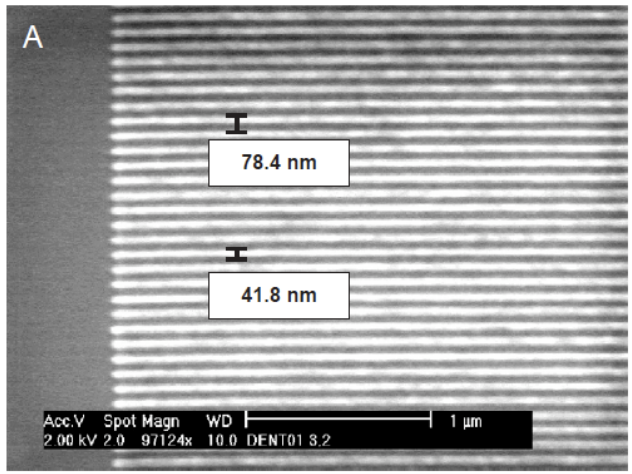

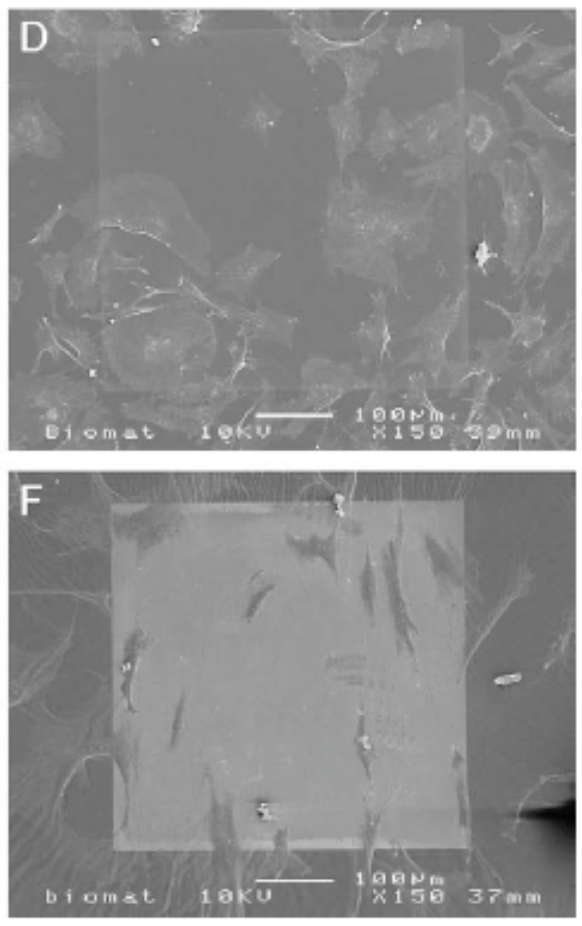

Máscaras feitas por litografia de feixe de elétrons para identificar o limite de sensibilidade dos fibroblastos.
D – 15 nm
F – 35 nm

Loesberg et al. Biomaterials V. 28 (2007) p. 3944-3951

Nanocordas

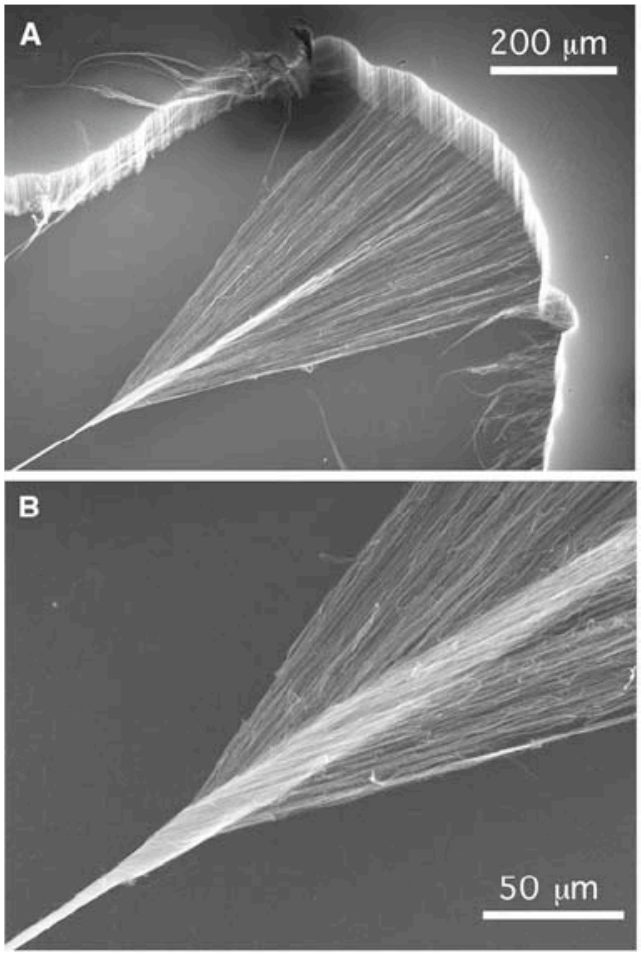

Fig. 1. (A and B) SEM images, at two different magnifications, of a carbon nanotube yarn in the process of being simultaneously drawn and twisted during spinning from a nanotube forest outside the SEM. The draw twist process was interrupted and the sample was transferred to a SEM for image recording. A forest strip (width ~600 μm) formed the pictured twisted yarn, 3.2 μm in diameter (fig. S2). The MWNTs, ~10 nm in diameter with length 10,000 times their width, form small bundles of a few nanotubes each in the forest, with individual nanotubes moving in and out of different bundles. The three-dimensional connectivity caused by intermittently switched bundling, visible in SEM micrographs, is believed to be important for the spinning process.

Zhang, M. et al.
Science 306, 2004, p. 1358-1361

Nanocordas

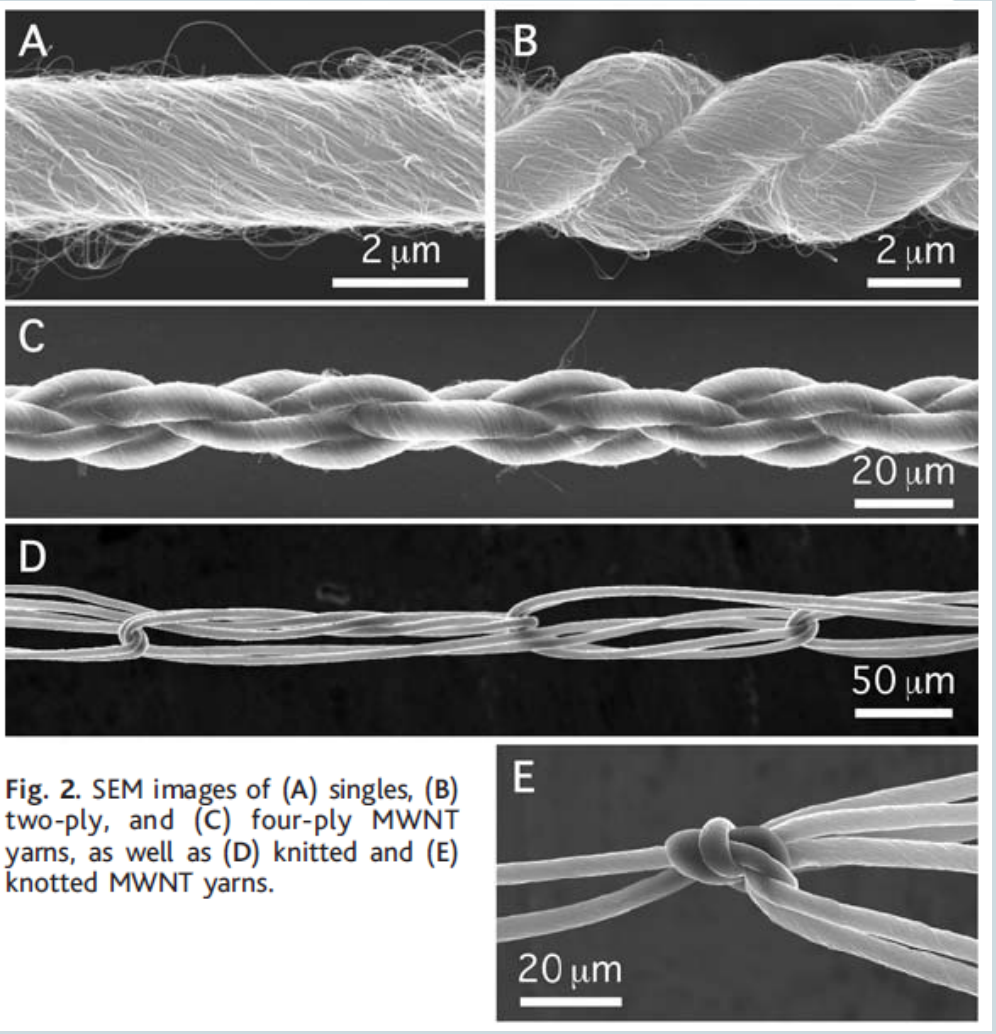

Fig. 2. SEM images of (A) singles, (B) two-ply, and (C) four-ply MWNT yarns, as well as (D) knitted and (E) knotted MWNT yarns.

Zhang, M. et al. Science 306, 2004, p. 1358-1361

Nanocordas

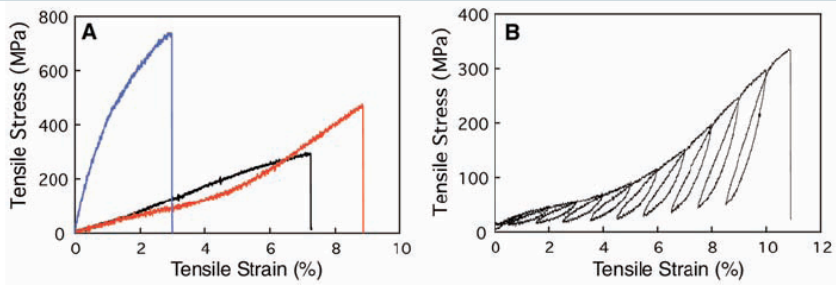

Fig. 3. Mechanical properties of MWNT yarns. (A) Engineering stress-strain curves of singles (black), two-ply (red), and PVA-infiltrated singles (blue) yarns at a strain rate of 1%/min for a centimeter gauge length. (B) Hysteretic stress-strain curves (strain rate 1%/min) observed on unloading and reloading a two-ply yarn over a 1.5% strain range after differing initial strains. (C) Energy loss per cycle for the stress-strain loops in (B) involving 1.5% strain change (blue squares) versus initial strain on unloading. Data for a similar experiment involving 0.5% strain change in the hysteresis loops are also shown (red circles). (D) Effective yarn moduli calculated for the stress-strain loops shown in (B) versus total tensile strain. Red circles and black squares are the effective moduli for the beginning and end of unloading, respectively; blue diamonds and green triangles are those for the beginning and end of reloading, respectively. (E) Percent change in diameter and length of a two-ply yarn (top) and a singles yarn (bottom) measured during yarn stretching in a SEM. Symbols: blue circles, initial stretch; black diamonds, first stress decrease; green circles, second stress increase; black squares, second stress decrease; red circles, stress increase until yarn rupture. Curves in (C) to (E) are guides for the eye.

Zhang, M. et al.
Science 306, 2004, p. 1358-1361

Nanofios de Si Células Fotovoltaicas

- Objetivos: flexibilidade mecânica, aumento na absorção e diminuição na quantidade de material

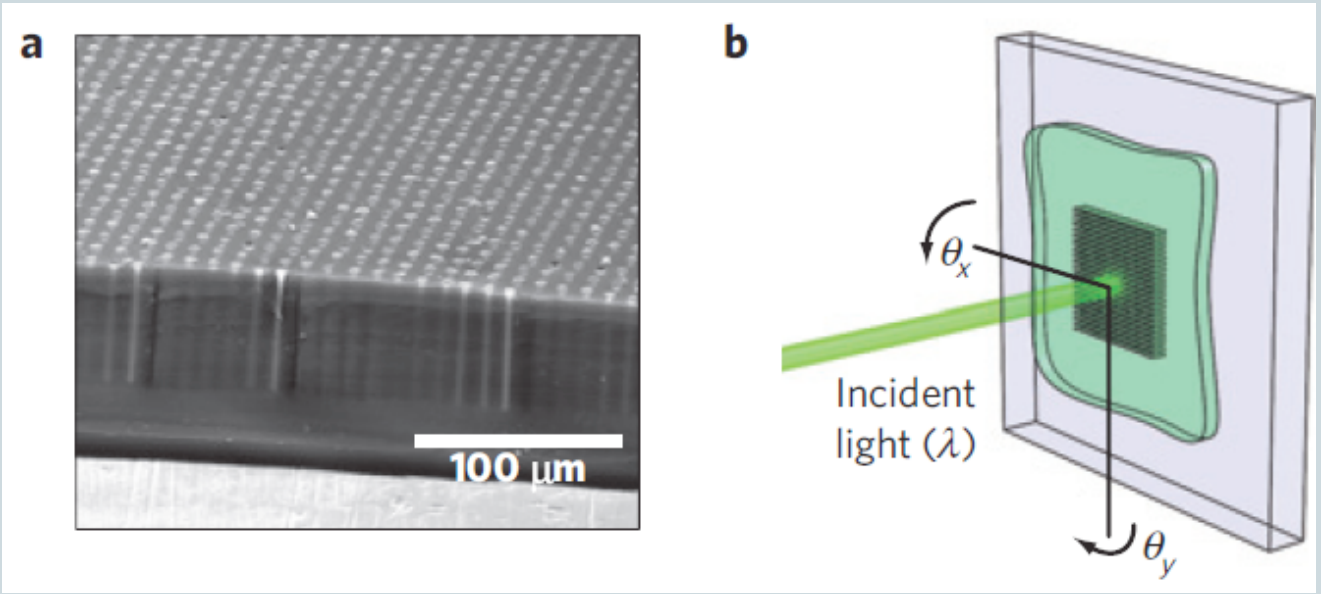

Nanofios de Si Células Fotovoltaicas

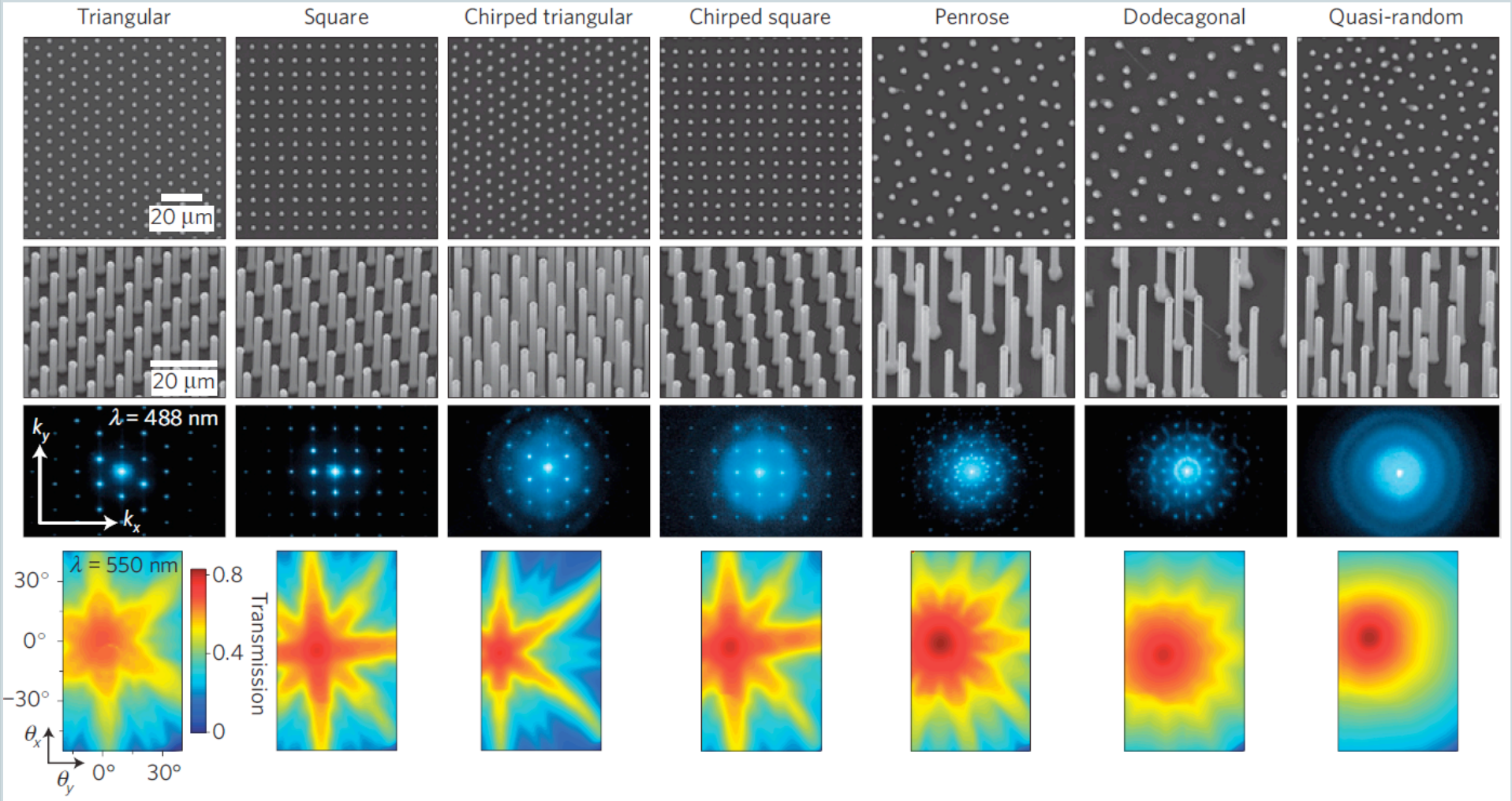

Cristais Fotônicos

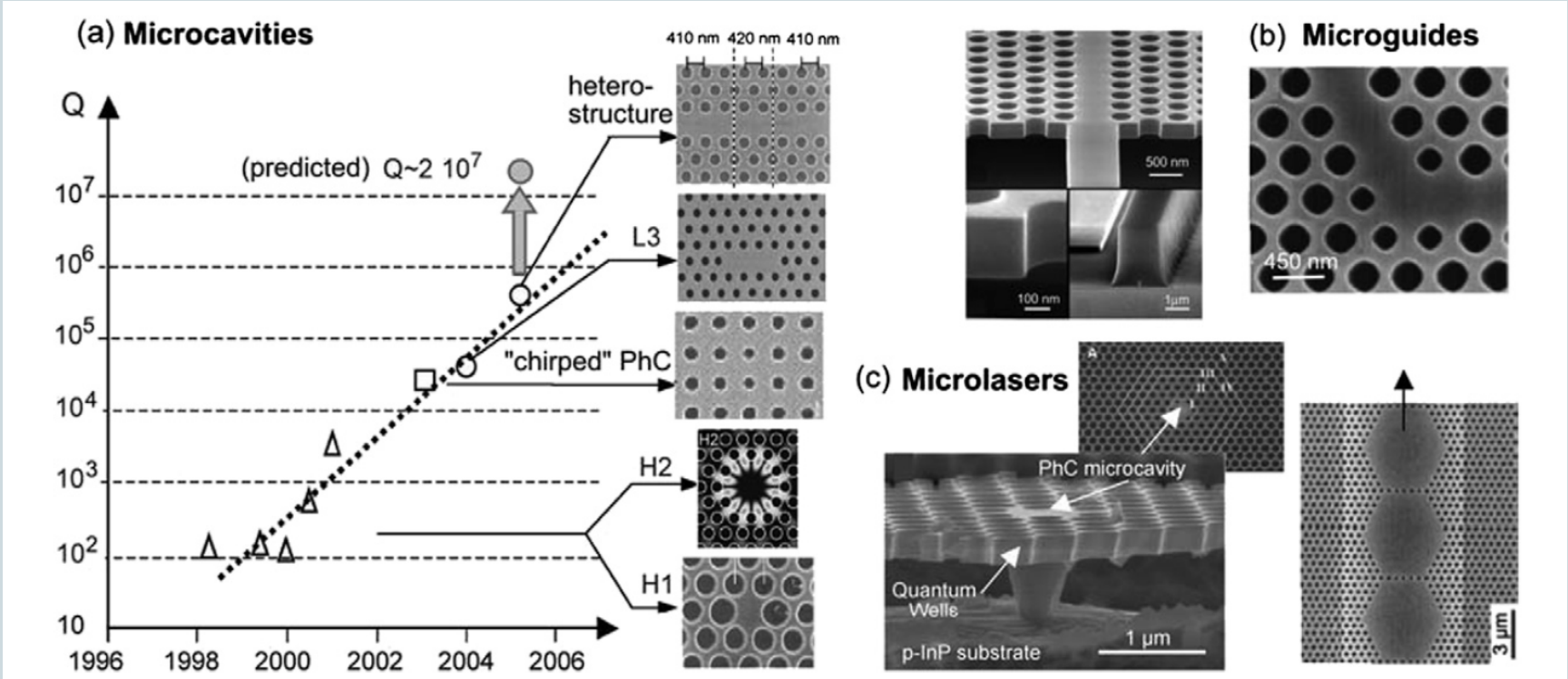

Fig. 1. Photonic crystal micro-devices. (a) Evolution of the Q-factor of photonic crystal microcavities during the last decade. (b) Left: W1 waveguide fabricated in the silicon membrane technology and formed by one row of missing holes in a hexagonal lattice of holes [33]. (b) Right: Light bent, realized in the same technology [5]. (c) Left: First electrically driven photonic crystal microcavity laser fabricated in the InP technology, the light being emitted vertically [6]. (c) Right: Edge-emitting coupled-cavity-waveguide laser fabricated on InP substrate [42].

Lourtioz 2008

Cristais Fotônicos

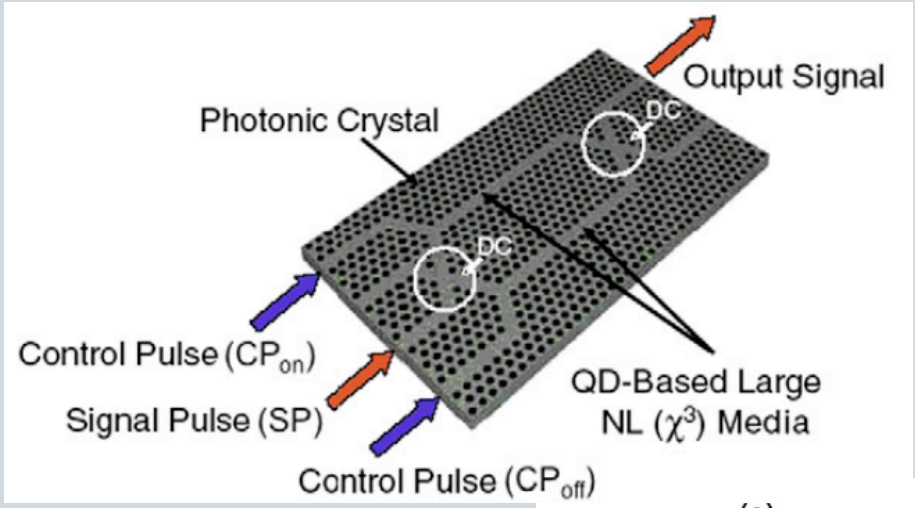

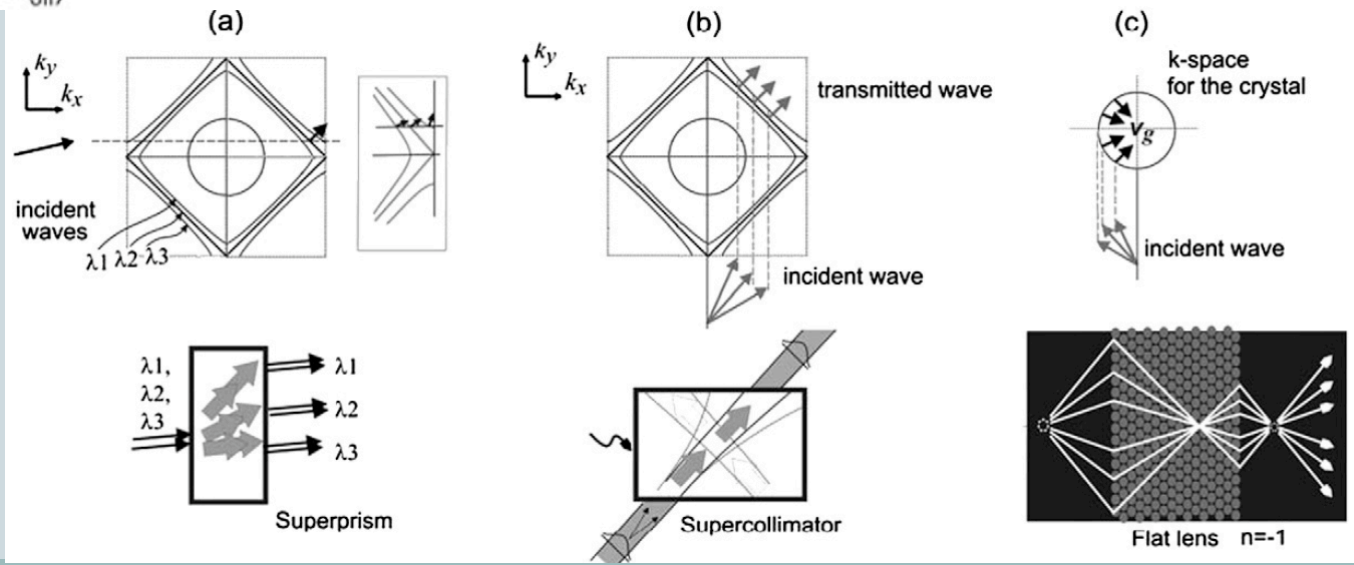

Cristais Fotônicos

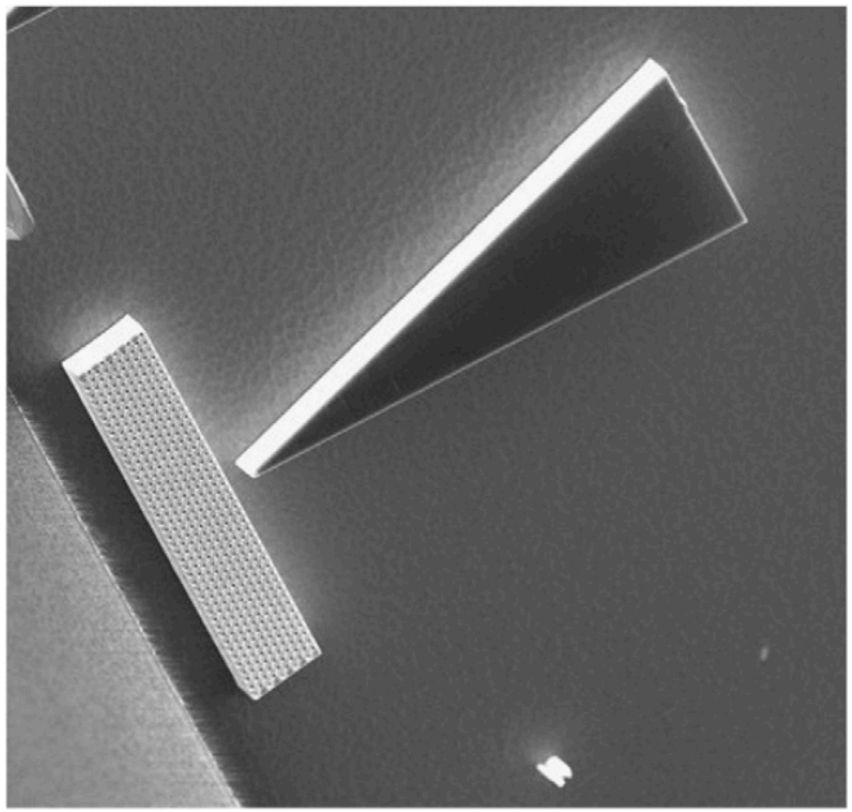

Fig. 16. SEM of a flat lens fed by a tapered optical waveguide.

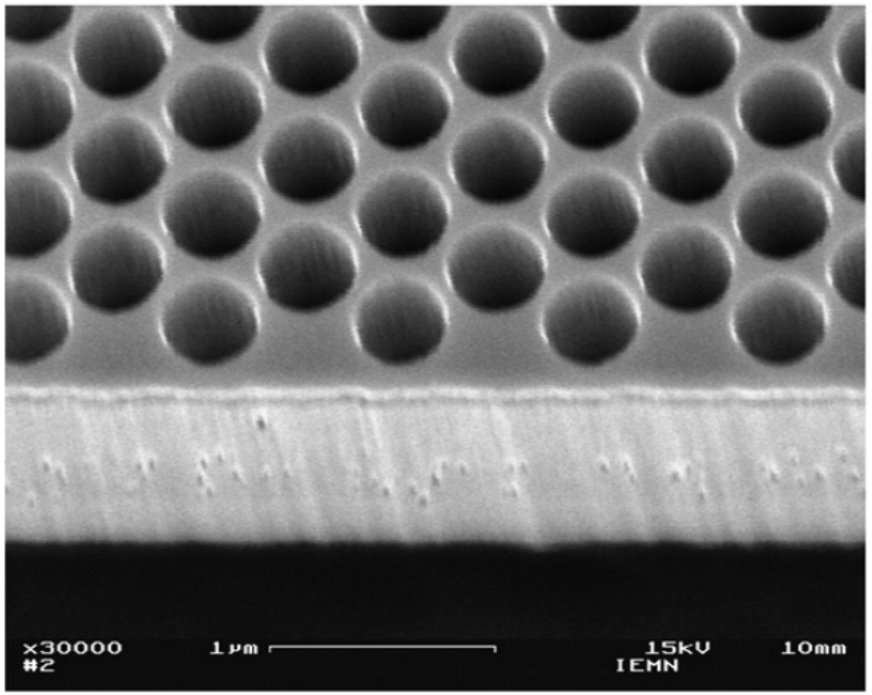

Fig. 15. Close up view of a hole array.

Lippens 2008

Metamateriais

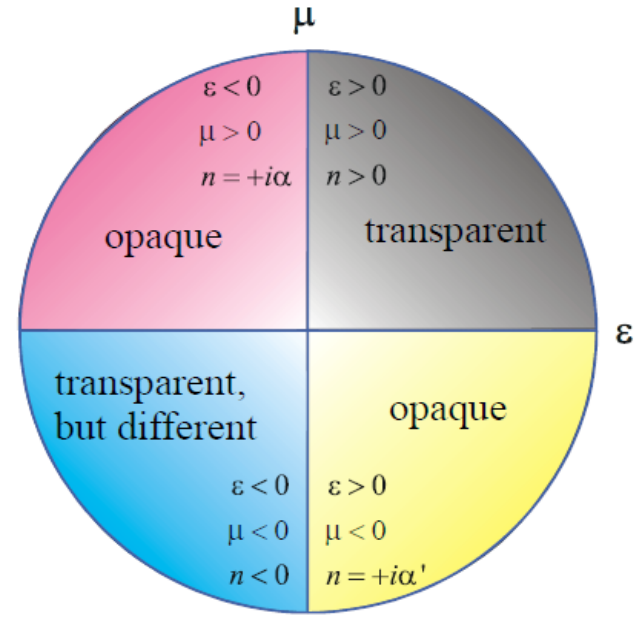

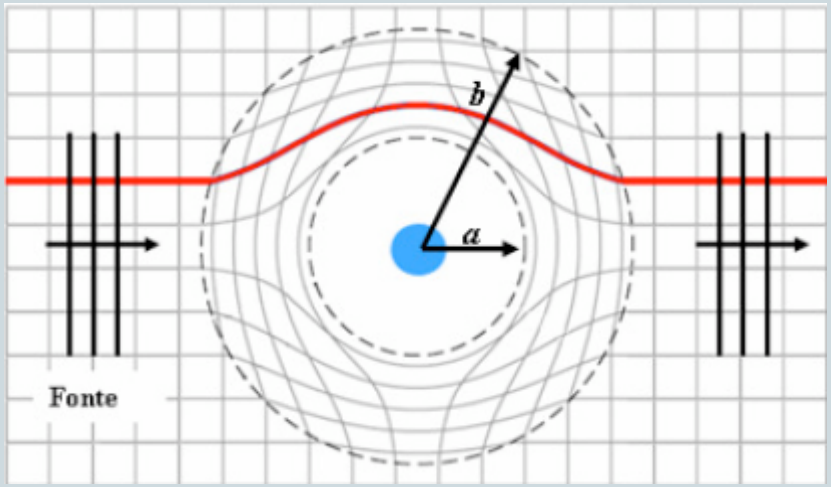

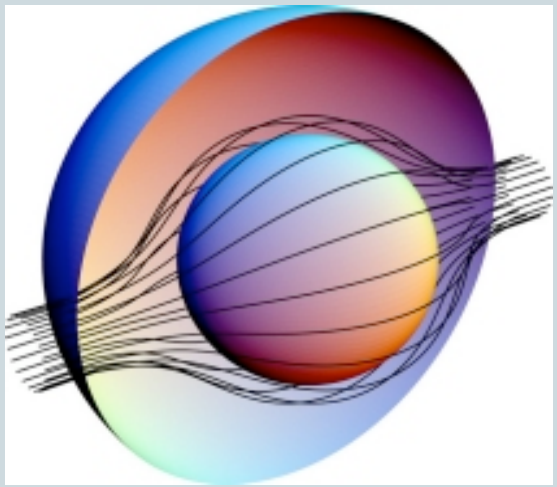

Uma aplicação: invisibilidade eletromagnética

Macedo 2008

Metamateriais

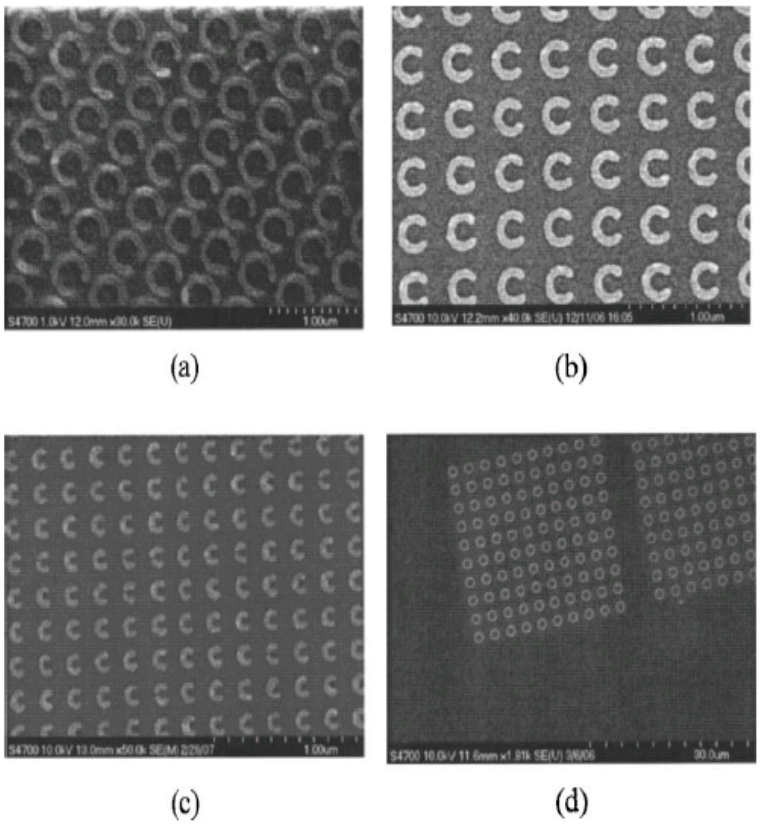

FIG. 2. Scanning electron micrographs of split ring arrays with radii (a) 215 nm, (b) 130 nm, and (c) 60 nm. (d) Scanning electron micrograph of complete 125 nm radius rings.

Sheridan et al. 2007

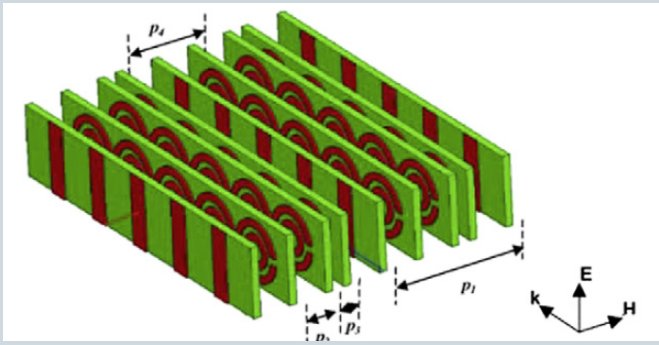

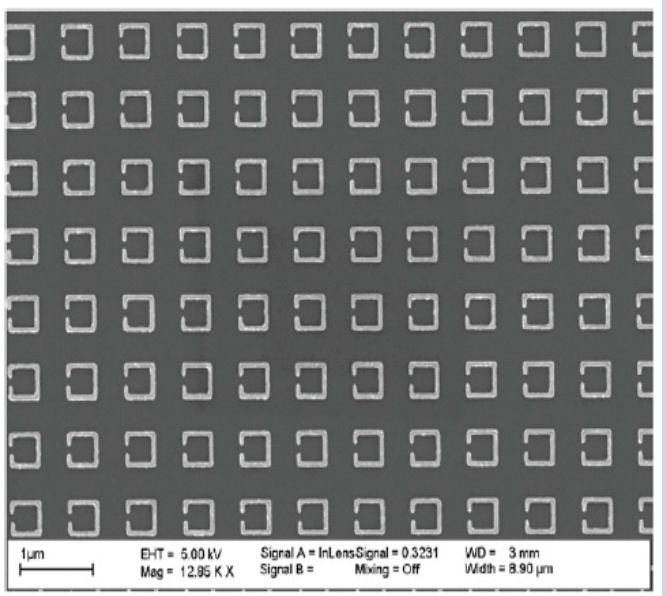

Fig. 11. SEM of a plasmon resonator array.

Lippens 2008

Metamateriais 3D

Michael , S. R. et al. Nature Materials 7 (2008) p. 543-546

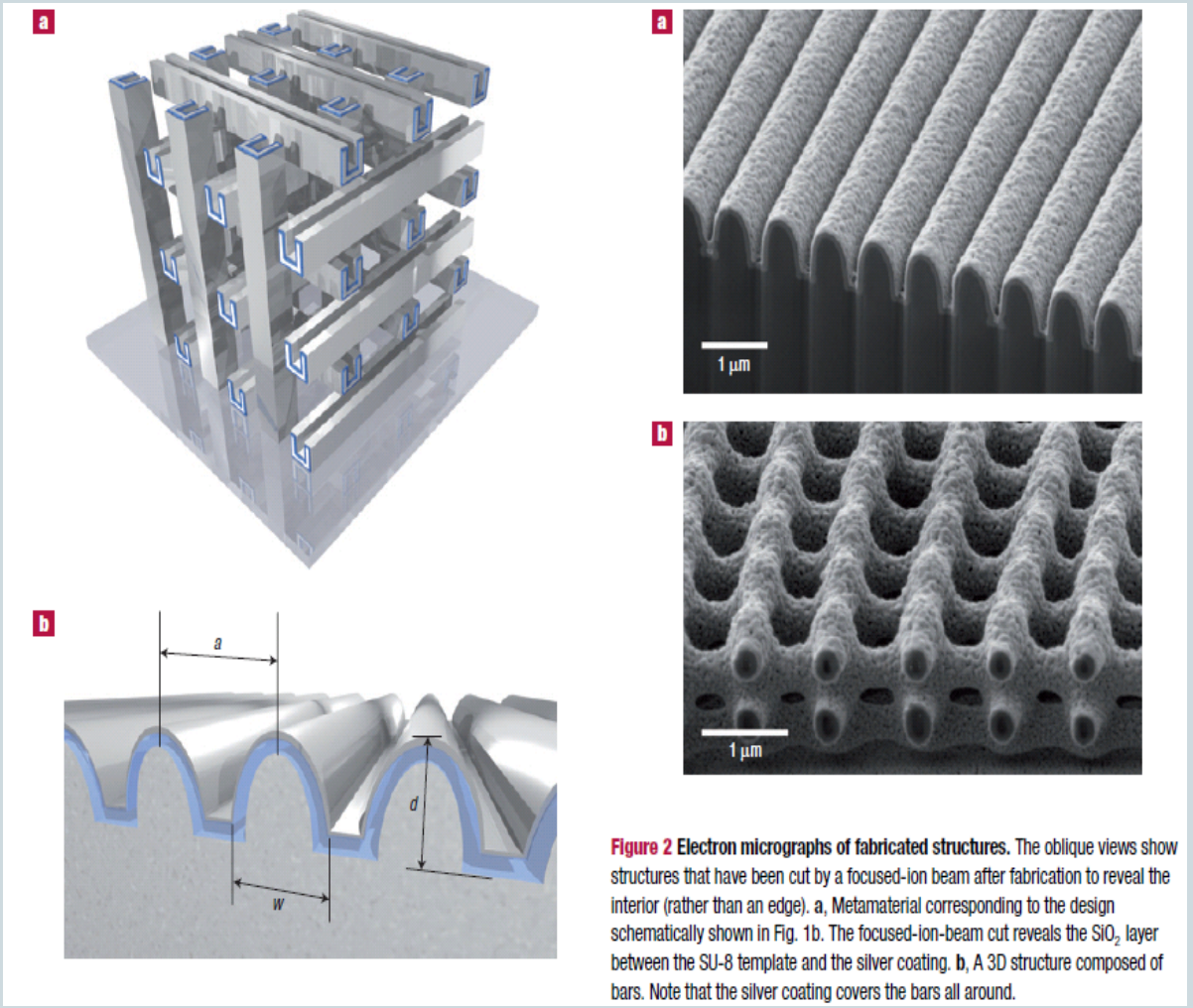

Figure 2 Electron micrographs of fabricated structures. The oblique views show structures that have been cut by a focused-ion beam after fabrication to reveal the interior (rather than an edge). **a**, Metamaterial corresponding to the design schematically shown in Fig. 1b. The focused-ion-beam cut reveals the SiO_2 layer between the SU-8 template and the silver coating. **b**, A 3D structure composed of bars. Note that the silver coating covers the bars all around.

Estruturas Quase-periódicas

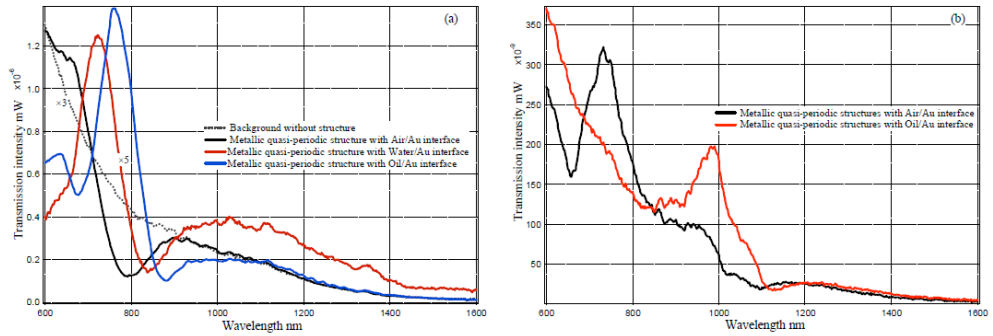

Fig. 3. The transmission spectra of the fabricated metallic quasi-periodic structures. (a) the quasi-periodic structures with three exposures at a rotation angle of 40° (the angle θ is 35°);(b)the quasi-periodic structures with four exposures at a rotation angle of 30° (the angle θ is 22°).

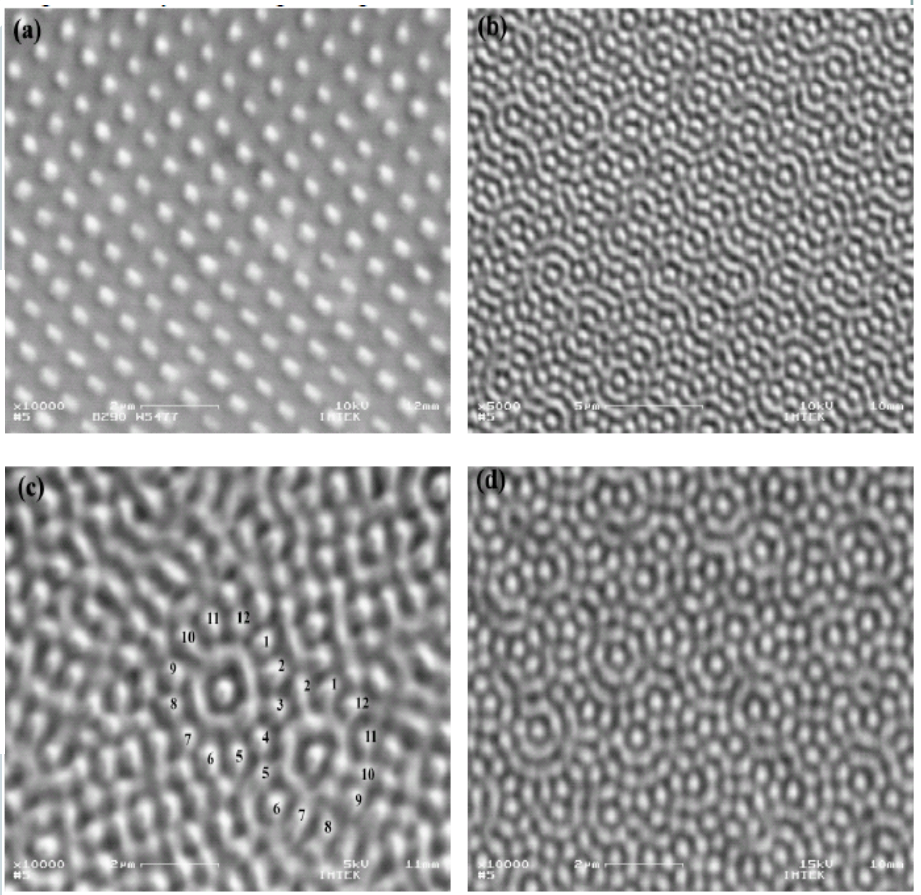

Fig. 2. SEM micrographs of fabricated metallic structures using the exposure wavelength at 442nm, (a),(b)&(c) the angle θ is 22°. (a) the fundamental 2D structures; (b) the quasi-periodic structures with three exposures at a rotation angle of 40°; (c) the quasi-periodic structures with four exposures at a rotation angle of 30°; (d) the quasi-periodic structures with three exposures at a rotation angle of 40° (the angle θ is 35°).

Wang 2008

Metamateriais Nanoporosos

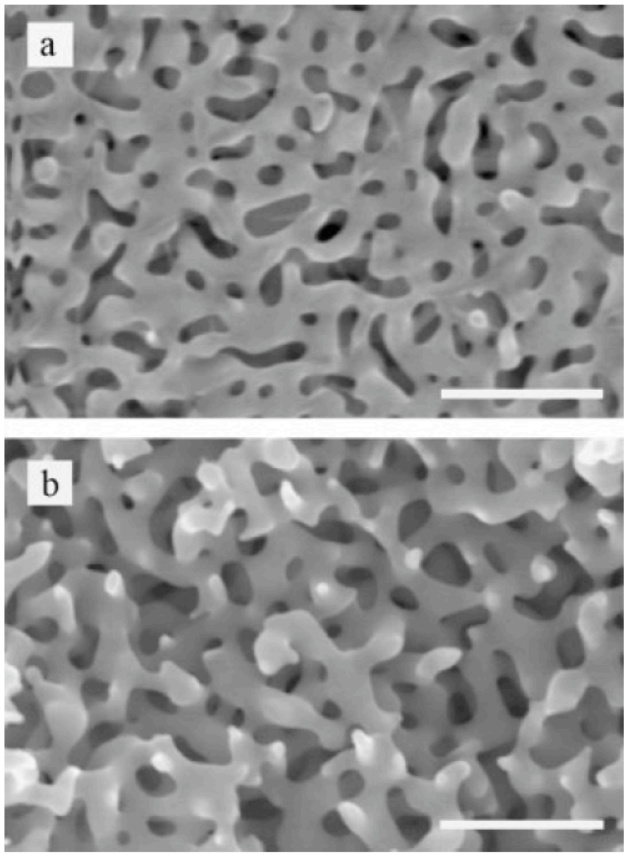

Figure 1. a) Plane-view, and b) cross-sectional scanning electron microscopy (SEM) images showing the characteristic spongelike open-cell foam morphology of np-Au. The material is very homogeneous and exhibits nanometer-sized pores and ligaments, the latter with a length-to-diameter aspect ratio close to one. The scale bars are 300 nm.

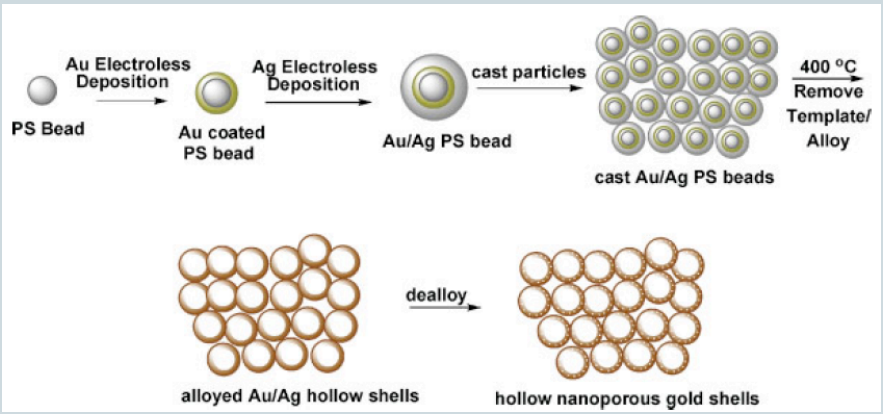

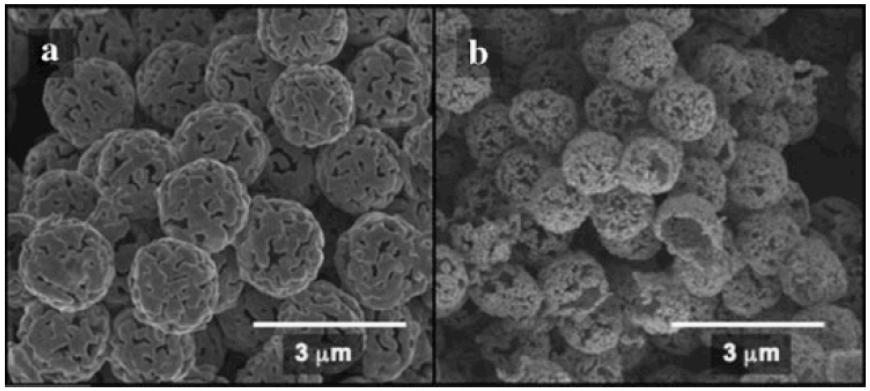

Figure 6. a) Fracture surface of a monolith containing hollow 1 μm $Ag_{0.7}Au_{0.3}$ shells before dealloying (density 1 g cm^{-3}). b) Fracture surface of a monolith containing hollow 1 μm nanoporous Au shells after dealloying (density 0.45 g cm^{-3} or 2.3% of the full density of Au).

Biener et al. 2008

Materiais Massivos Nanoestruturados

- Definição
  - Materiais monofásicos ou multifásicos organizados em unidades entre 1 e 200 nm
- Motivação
  - A grande densidade de contornos de grão altera significativamente:
    - limite de escoamento
    - módulo de elasticidade
    - ductilidade
    - tenacidade
    - resistência à fadiga
    - resistência à fluência

Equação de Hall-Petch

$\sigma_{esc} = \sigma_o + K_e (d)^{-n}$

n é tradicionalmente 1/2

Propriedades

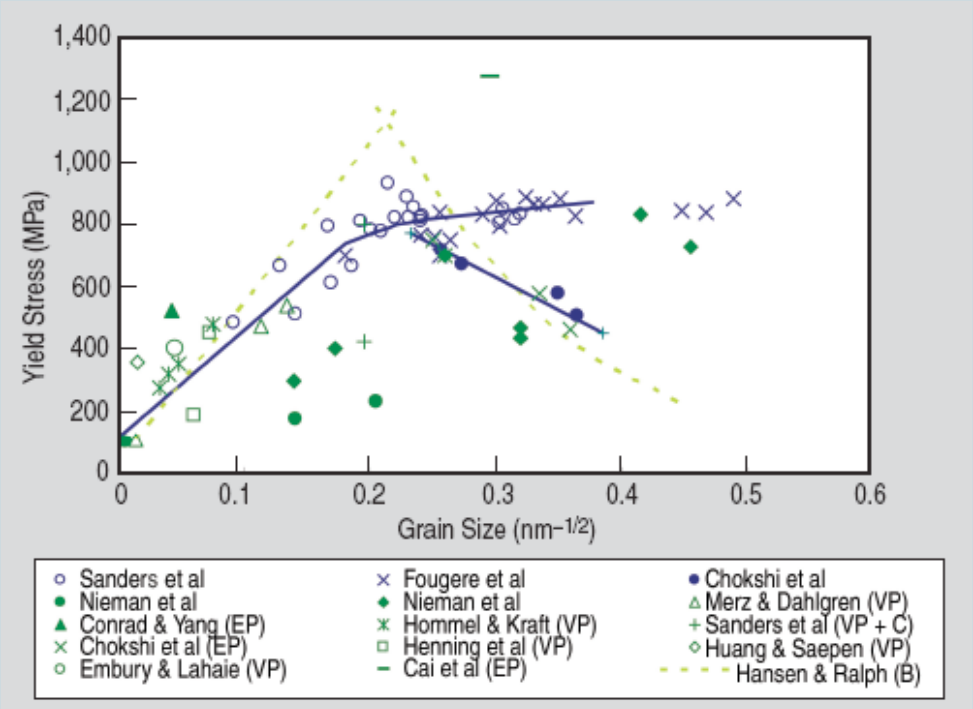

Limite de Escoamento do Cobre

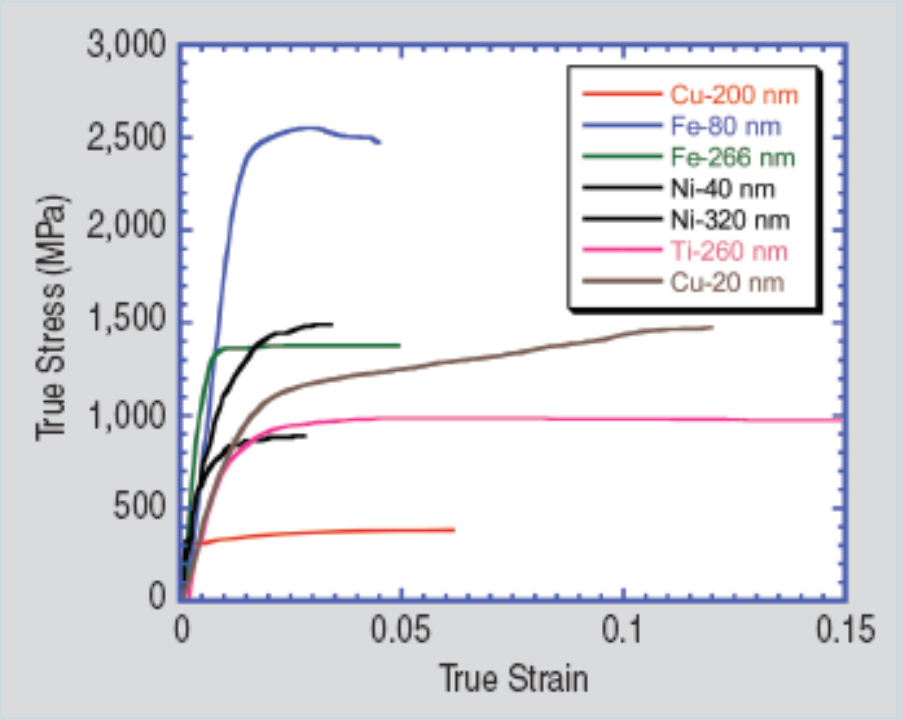

Curva Tensão x Deformação compressiva

Meyers et al, JOM, Abril (2006) p. 41-48

Controle Nanoestrutural

- Processamento
  - Métodos “Botton-up”
    - Técnicas de deposição
    - Técnicas de compactação
  - Métodos “Top-down”
    - “Torsion straining under High Pressure” (HPT)
    - “Equal Channel Angular Pressing” (ECAP)

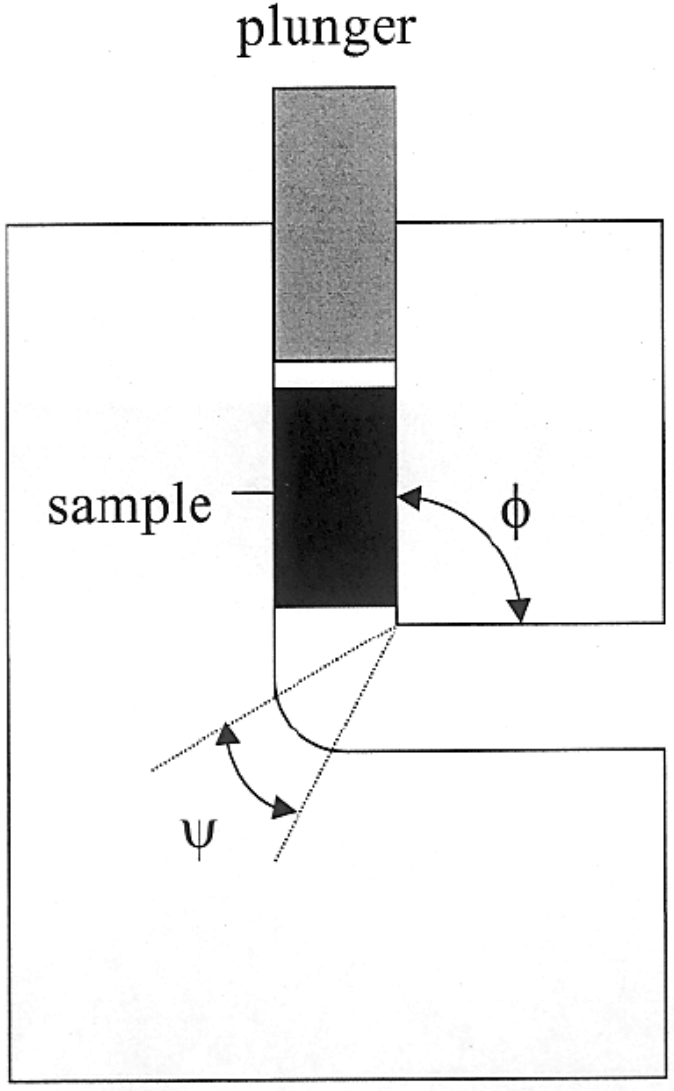

Segal, V. M. Mat. Sci. Eng. A197 (1995) p. 157-164
Park, K-T et al. Mat. Sci Eng. A293 (2000) p. 165-172

Ti com Grão Ultrafino

- Rota B_C
- Grãos equiaxiais
- TG ~ 260 nm

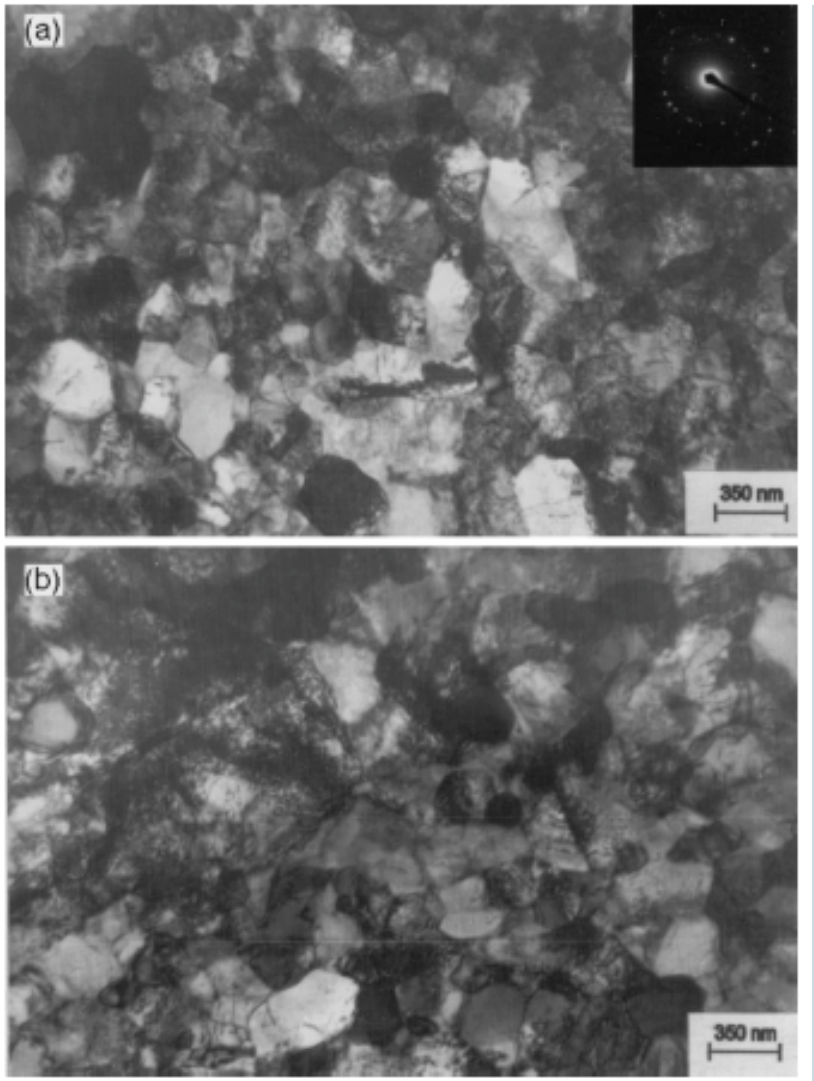

Stolyarov, V.V. et al. Mat Sci Eng A299 (2001) p. 59-67

Estratégias para contornar a ausência de encruamento

- Distribuição bimodal de TG

A – Cu recristalizado
B – Cu deformado 95%
C – Cu deformado 93% N Liq
D – C + 180ºC / 3 min
E – C + 200ºC / 3 min

D

E

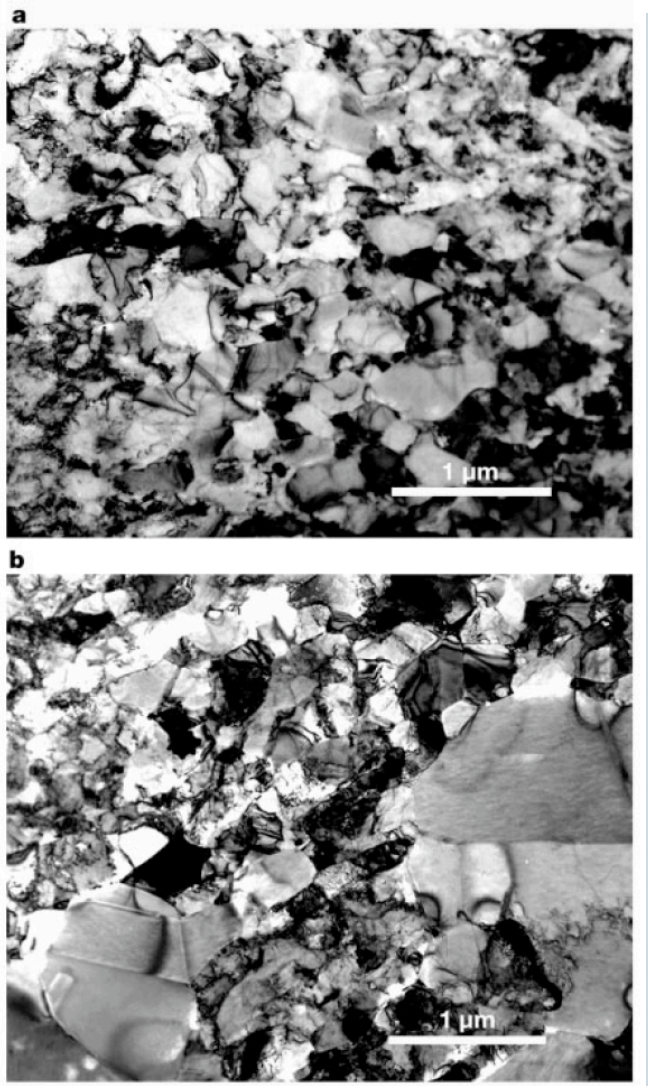

Wang, Y et al, Nature, V. 419/31 (2006) p. 912-915

Estratégias para contornar a ausência de encruamento

- Distribuição bimodal de TG

A – Cu recristalizado
B – Cu deformado 95%
C – Cu deformado 93% N Liq
D – C + 180ºC / 3 min
E – C + 200ºC / 3 min

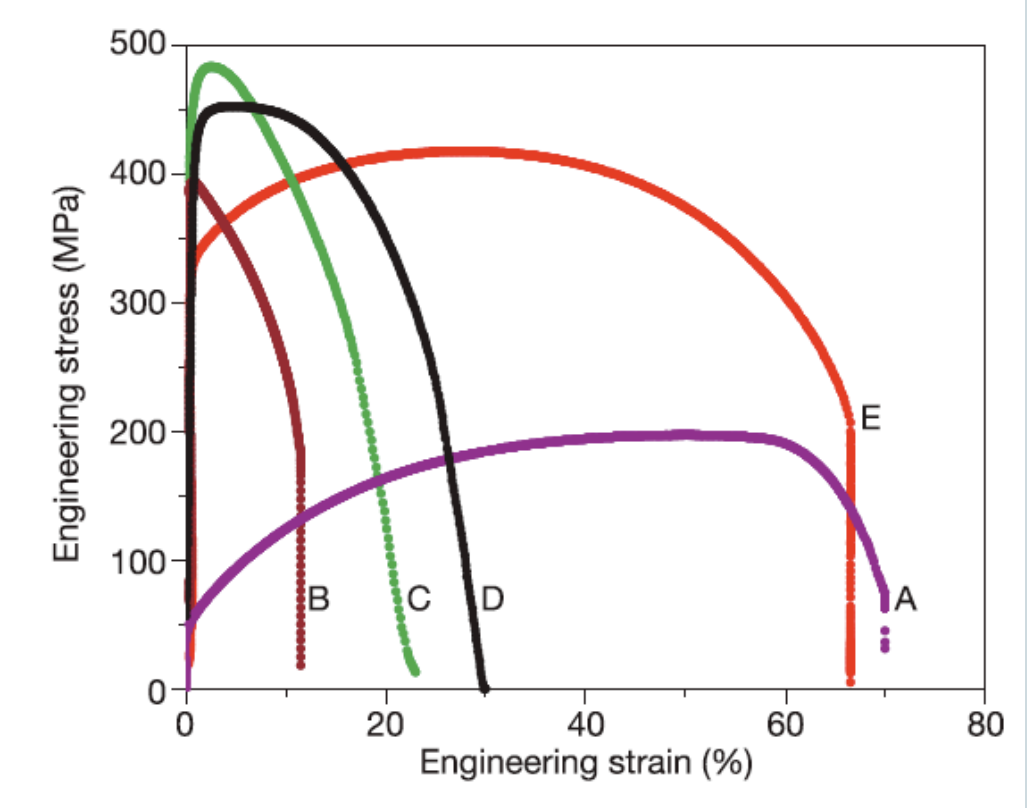

Wang, Y et al, Nature, V. 419/31 (2006) p. 912-915

Estratégias para contornar a ausência de encruamento

- Nanomaclas

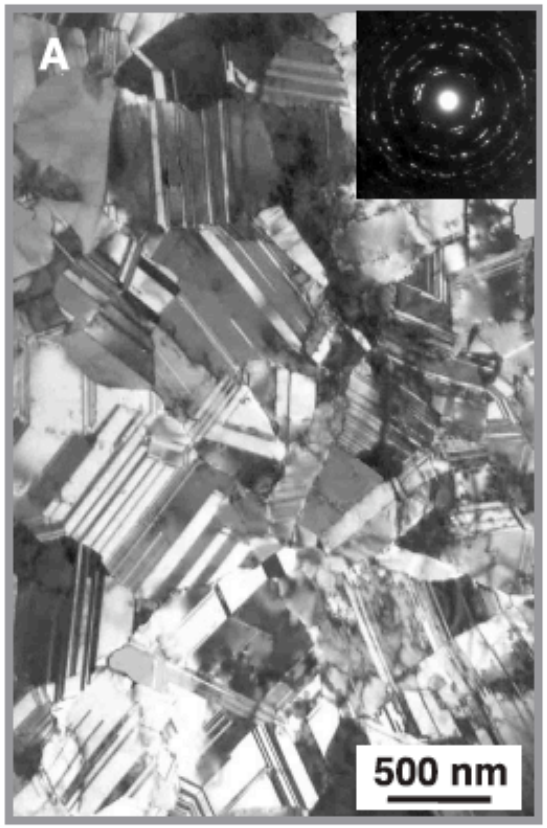

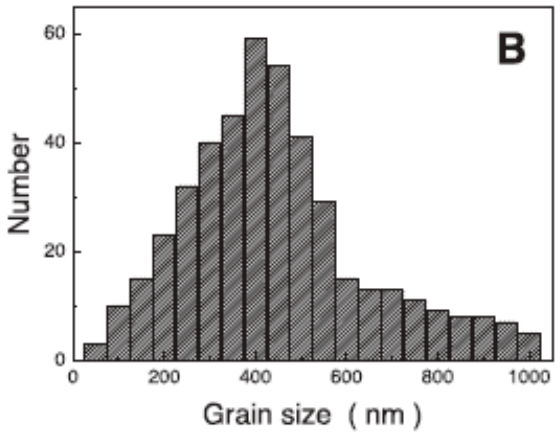

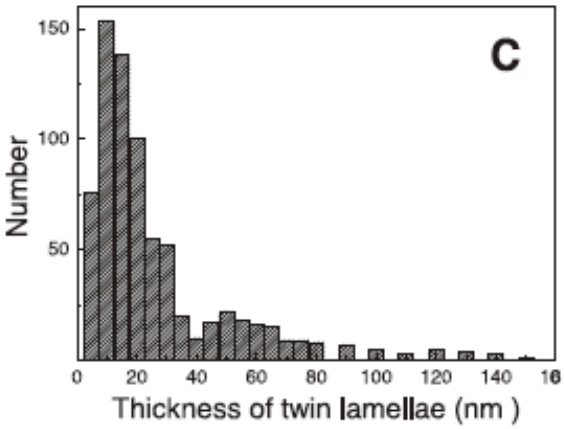

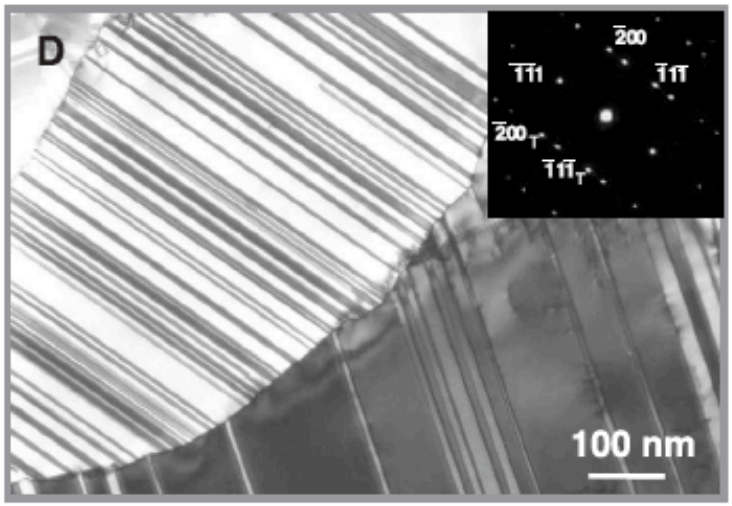

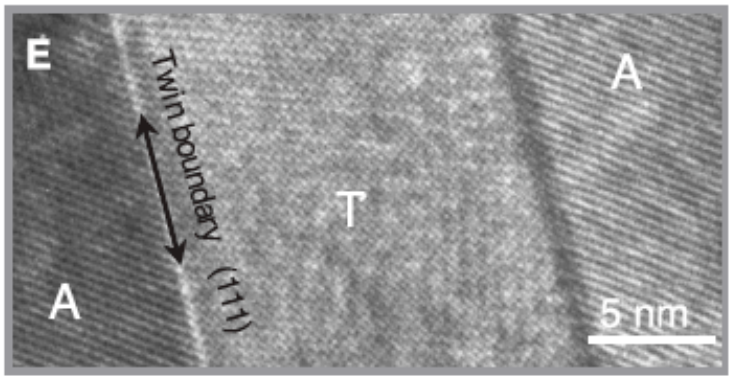

Lu, L. et al, Science, V. 304 (2004) p. 422-426

Estratégias para contornar a ausência de encruamento

- Nanomaclas

Maclas são efetivas no bloqueio do movimento das discordâncias.

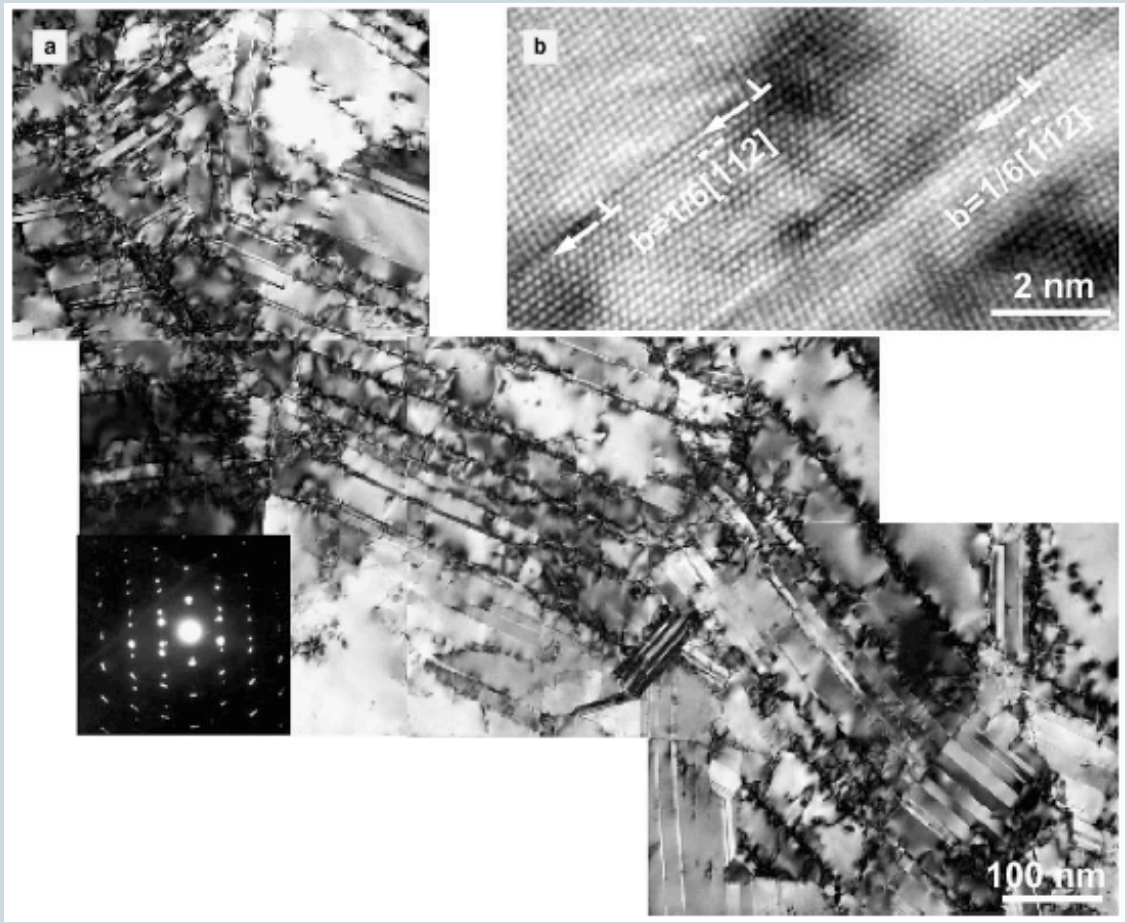

Shen, Y. F. et al, Scripta Mater, V. 52 (2005) p. 989-994

Estratégias para contornar a ausência de encruamento

- Nanomaclas

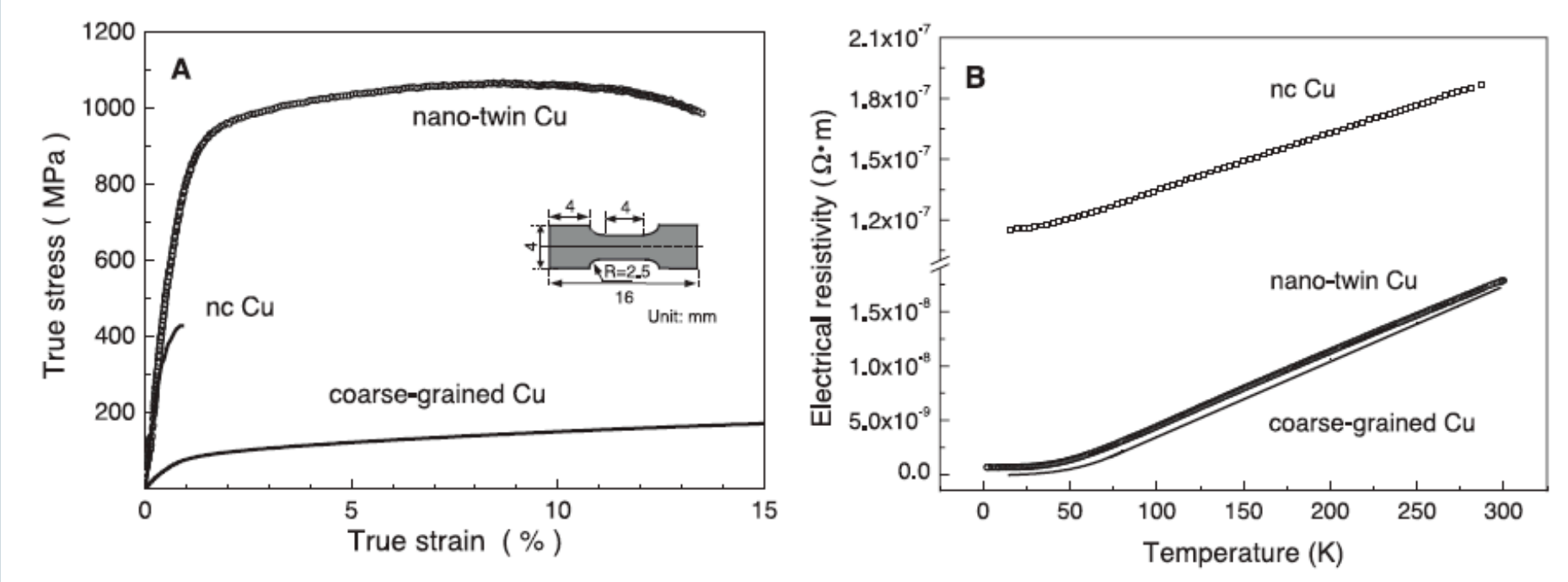

Lu, L. et al, Science, V. 304 (2004) p. 422-426

Ti Nanocristalino como Biomaterial

State	UTS (MPa)	YS (MPa)	*A* (%)	*Z* (%)
Initial	440	370	38	60
ECAP, 4 passes	630	545	22	51
ECAP, 4 passes + TMT $\varepsilon = 60\%$	1030	845	12	51
ECAP, 4 passes + TMT $\varepsilon = 80\%$	1150	1100	11	56

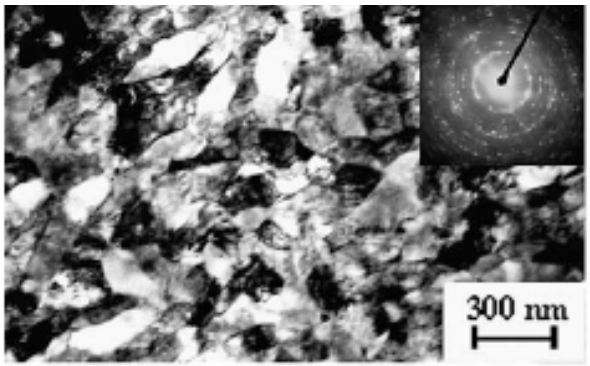

Seção transversal

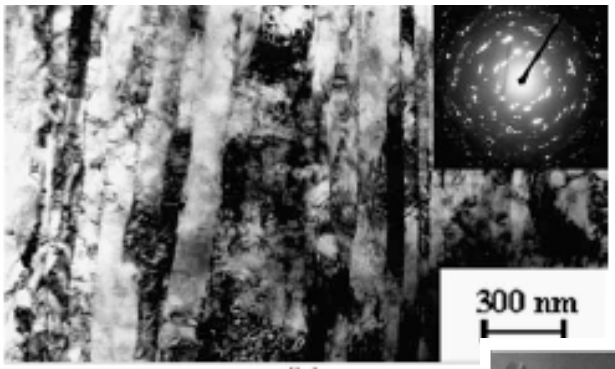

Seção longitudinal

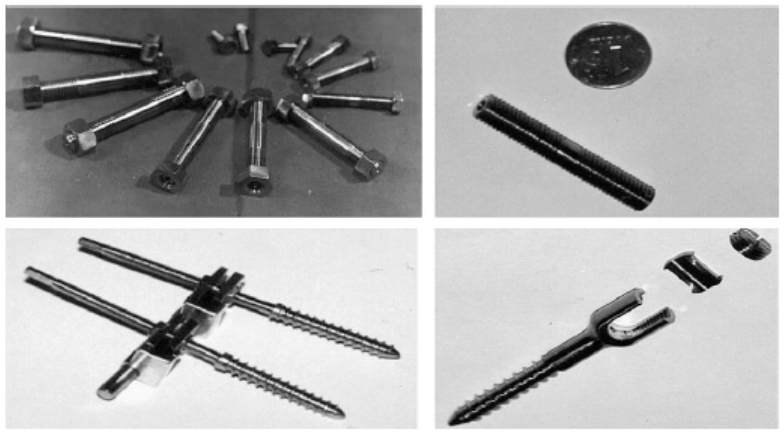

Latysh, , V. et al, Current Applied Physics V.6 (2006) p. 262-266

Controle Nanoestrutural

- Estabilização da estrutura
  - Abordagem cinética
    - Contornos de grão têm sua mobilidade reduzida por arraste de segunda fase e soluto.
  - Abordagem termodinâmica

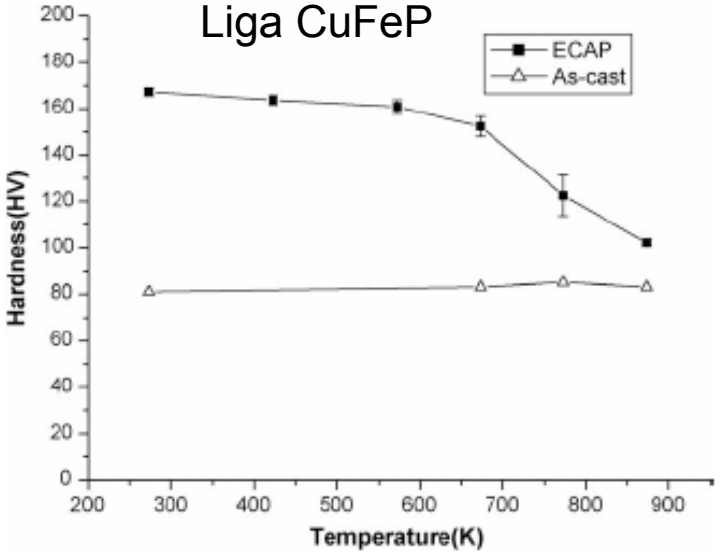

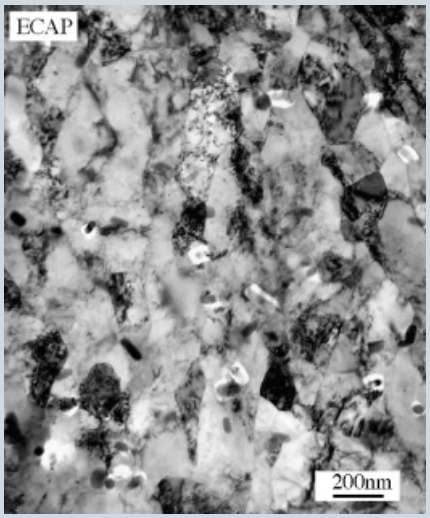

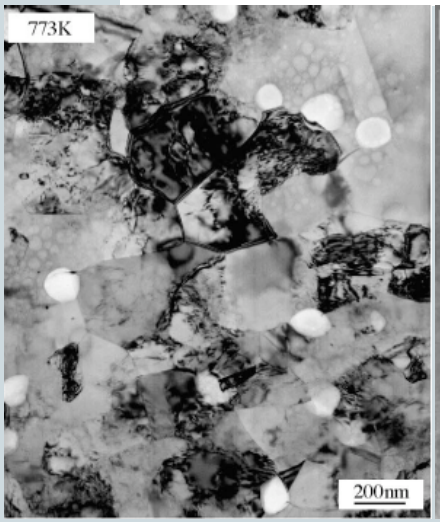

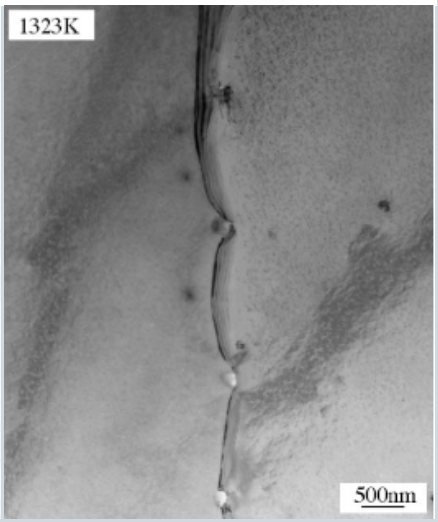

Cao, H. et al. Mat. Sci. Eng. A431 (2006) p. 86-91

Controle Nanoestrutural

- Estabilização da estrutura
  - Abordagem cinética
  - Abordagem termodinâmica
    - Força motriz para o crescimento de grão é reduzida pela redução da energia do contorno de grão através da saturação do mesmo.

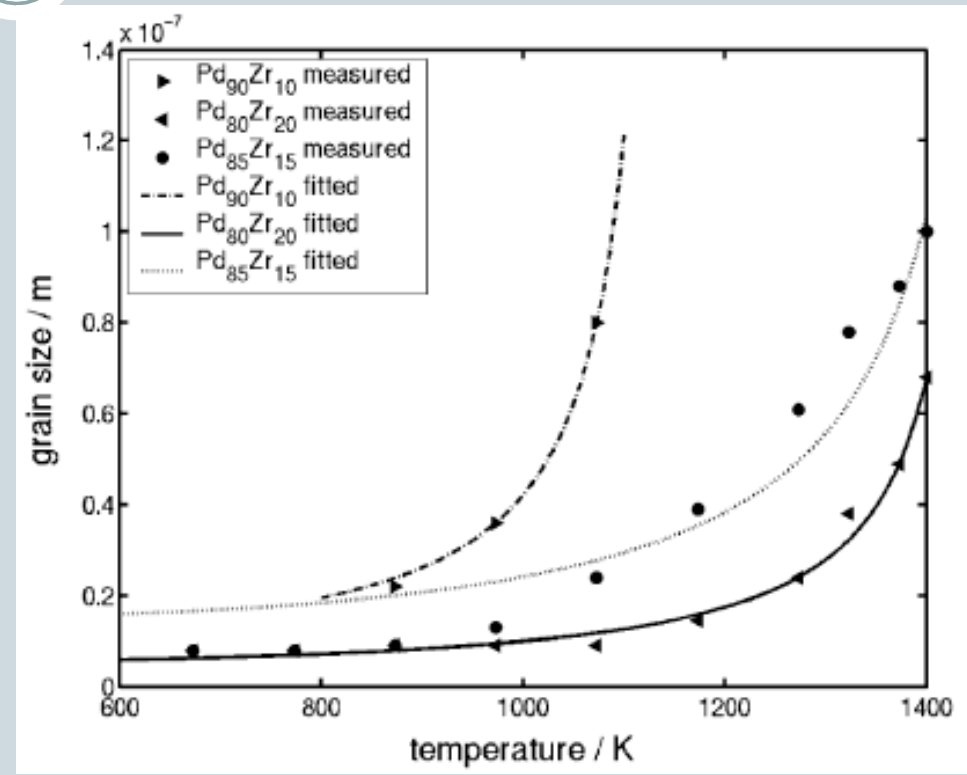

TG saturado

$$D = \frac{3\Gamma_{b0} V_M}{X_{total} - \exp\left(\frac{\sigma_0 - \Gamma_{b0}\Delta H_{seg}}{\Gamma_{b0} RT}\right)}$$

Liu e Kirchheim, Scr. Mater. 51 (2004) p. 521-525

Sensores de Bragg

- Redes de Bragg em POF
  - Sensores na ponta de POF através de redes de Bragg constituídas de multicamadas de óxidos com diferentes índices de refração

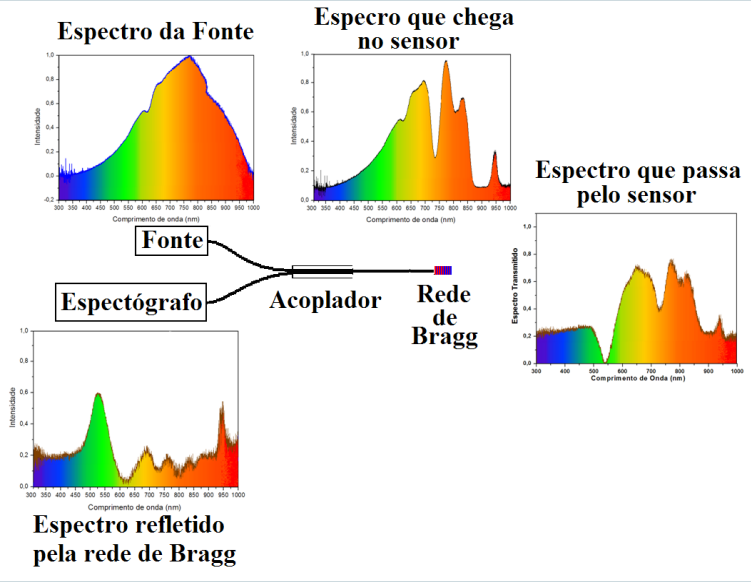

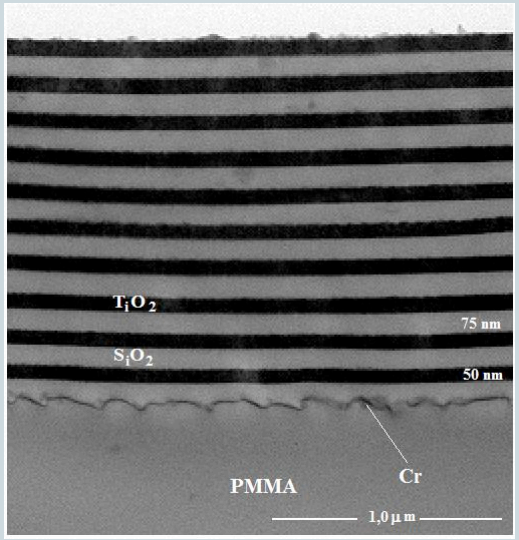

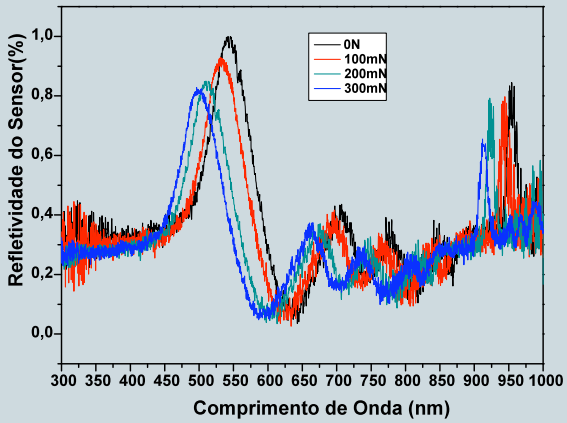

Revestimento Cerâmico Nanoestruturado Multicomponente

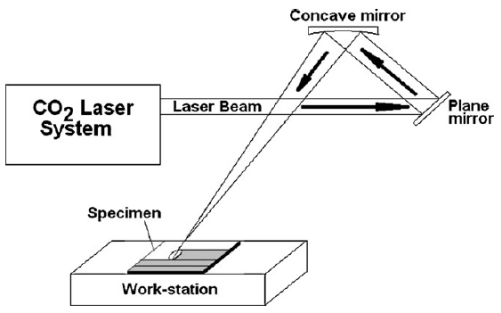

Pó de Al, TiO_2 e B_4C colocado sobre a superfície; sinterização SHS (self-propagating high temperature synthesis) proporcionada pelo feixe de laser

Masanta et al. (2009)

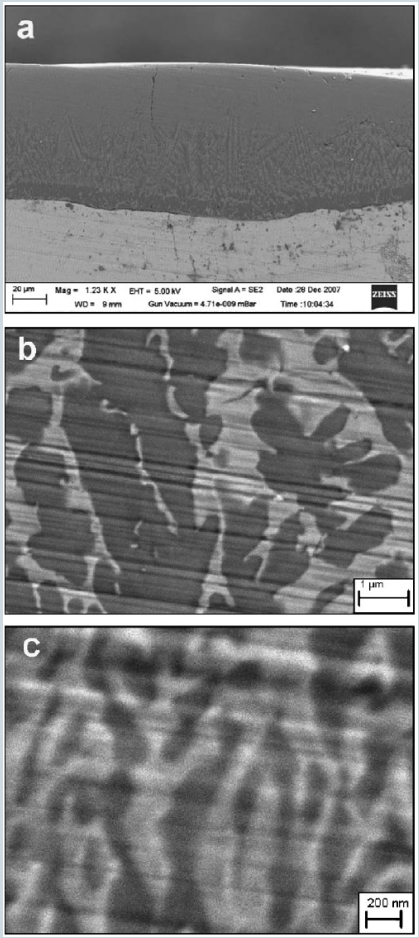

2,5 kW a 2,5 mm/s

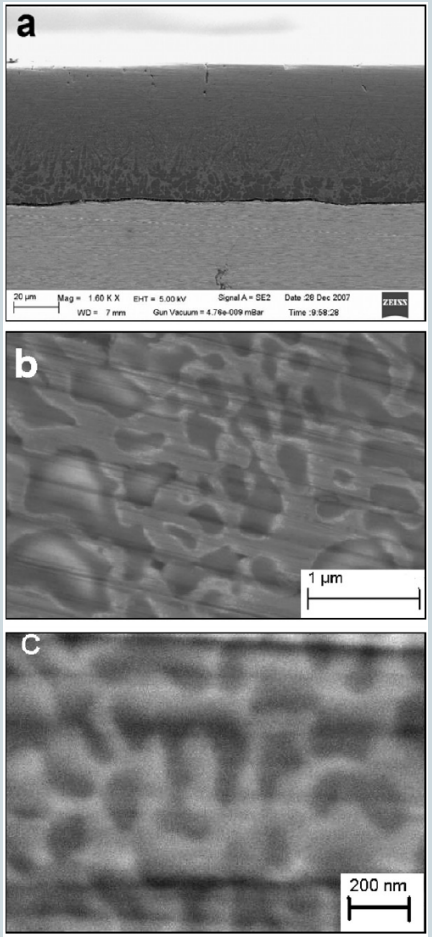

2,5 kW a 5 mm/s

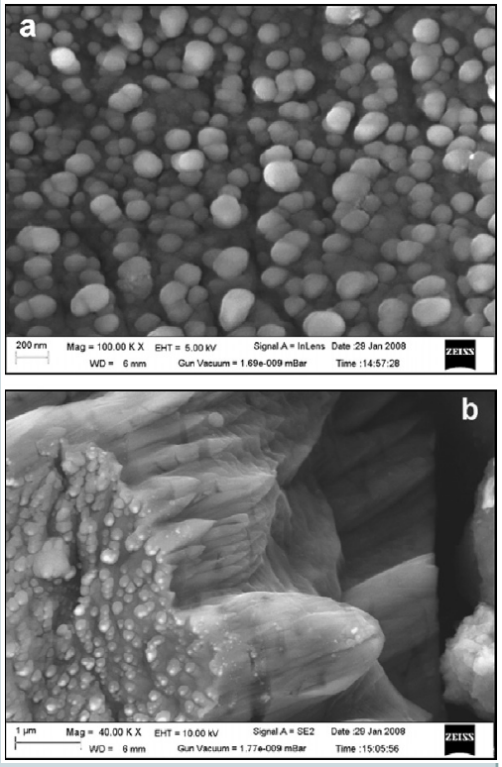

2,5 kW a 10 mm/s

Revestimento Cerâmico Nanoestruturado Multicomponente

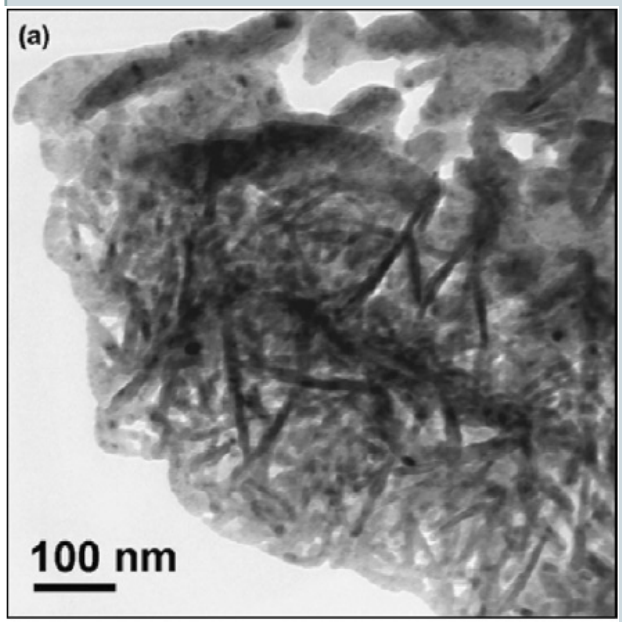

Campo claro

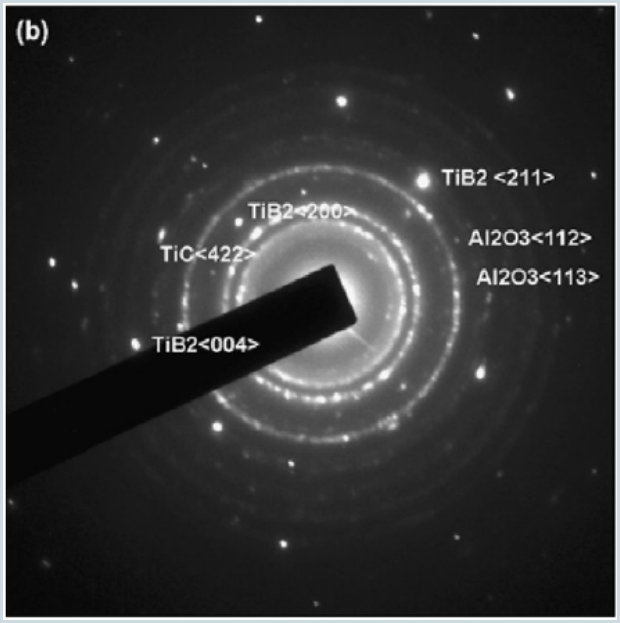

SAD

2,5 kW a 10 mm/s

Masanta et al. (2009)

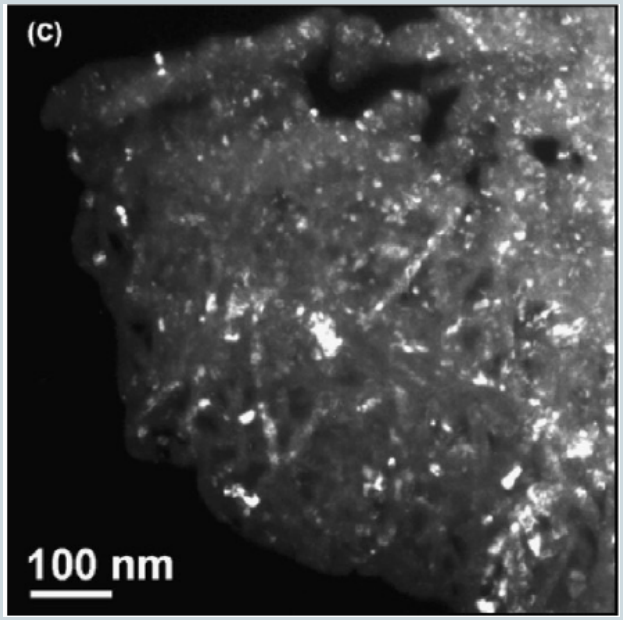

Campo escuro com o spot de TiB_2

Revestimento de Ti sobre Vidro Metálico Zr10Al5Ni30Cu

Deposição por sputtering a 200ºC

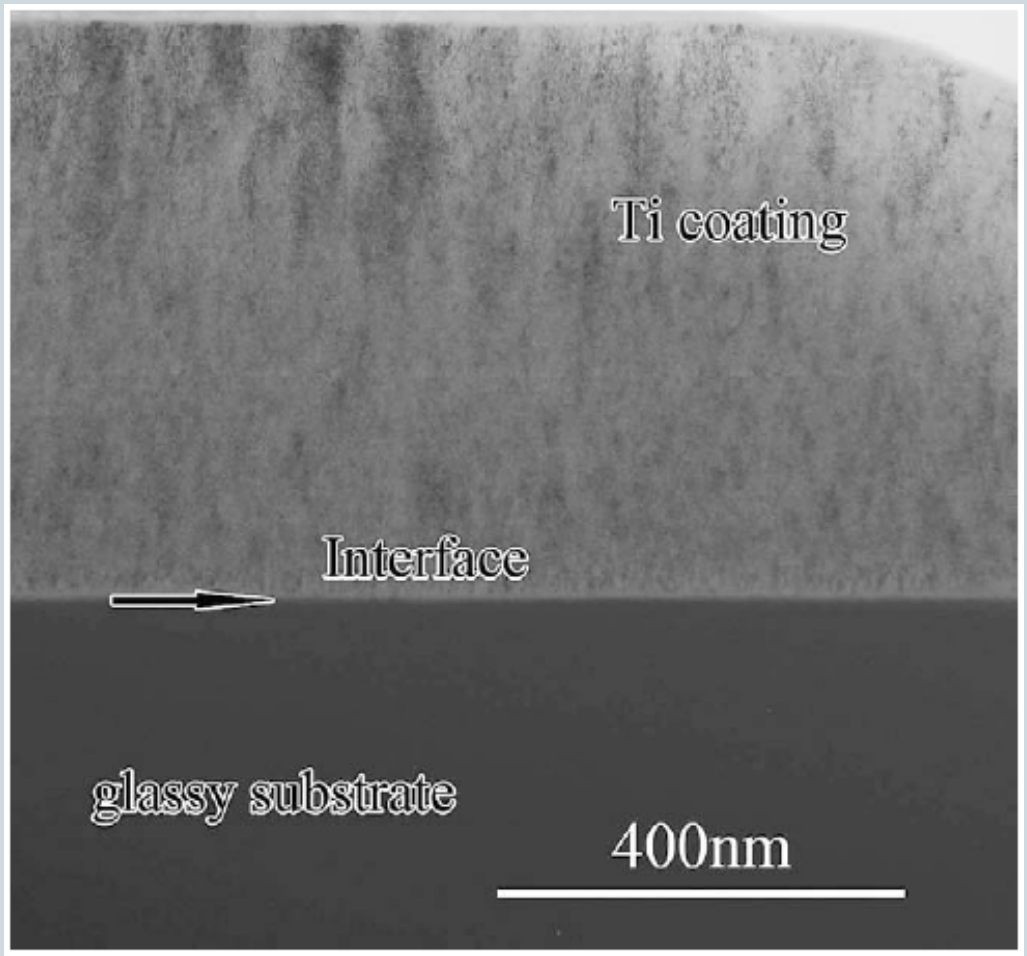

Qin et al. 2009

Revestimento de Ti sobre Vidro Metálico Zr10Al5Ni30Cu

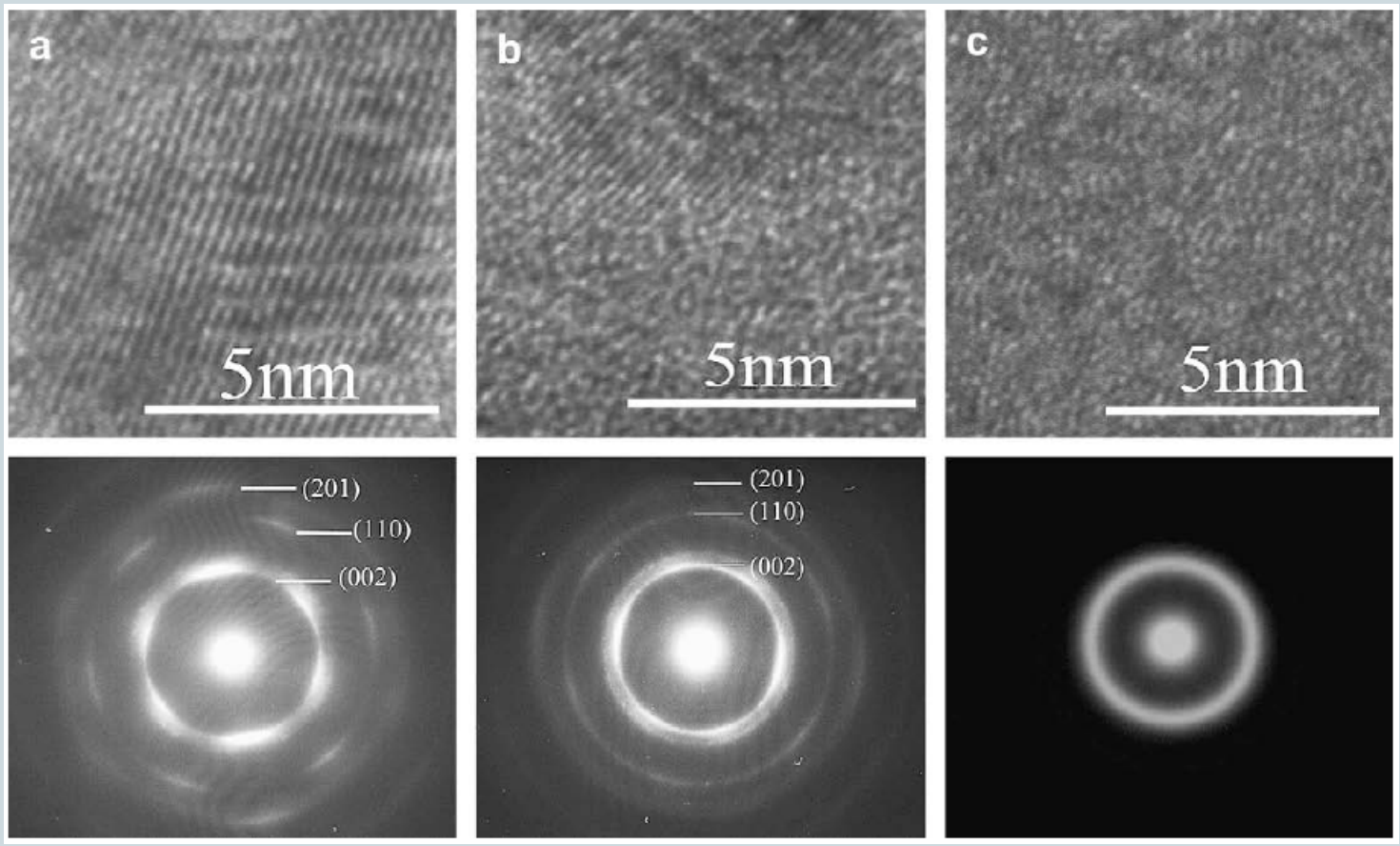

Revestimento Interface Vidro

Qin et al. 2009

Multiferróicos – $BiFeO_3$

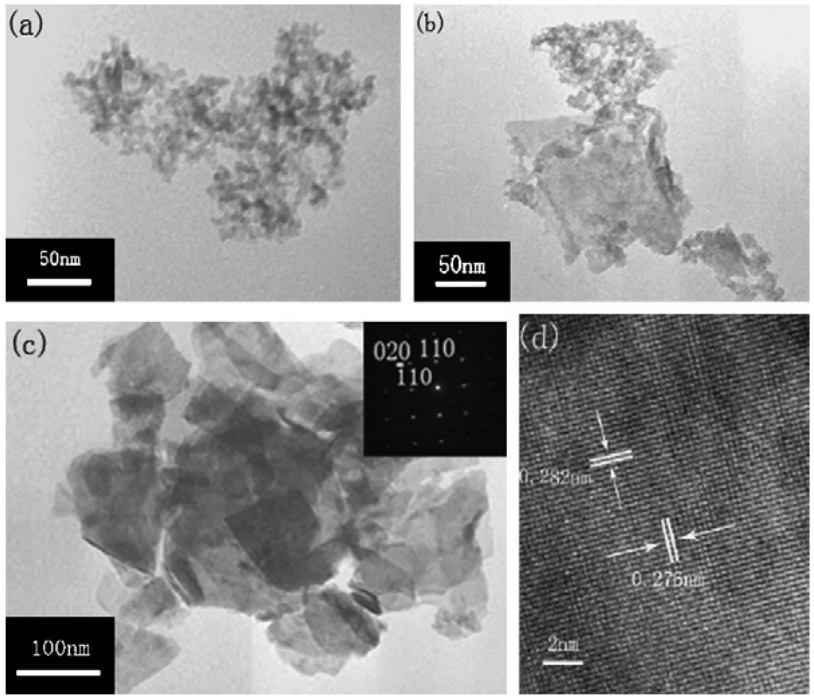

Fig. 2. Transmission electron microscope images of the as-prepared samples synthesized by the potassium nitrate-assisted hydrothermal process at 200 °C for (a) 24 h, (b) 36 h, and (c) 48 h, respectively, and electron diffraction pattern of a chosen randomly nanoflake (inset). (d) High-resolution TEM (HRTEM) image of one randomly chosen BFO nanoflake.

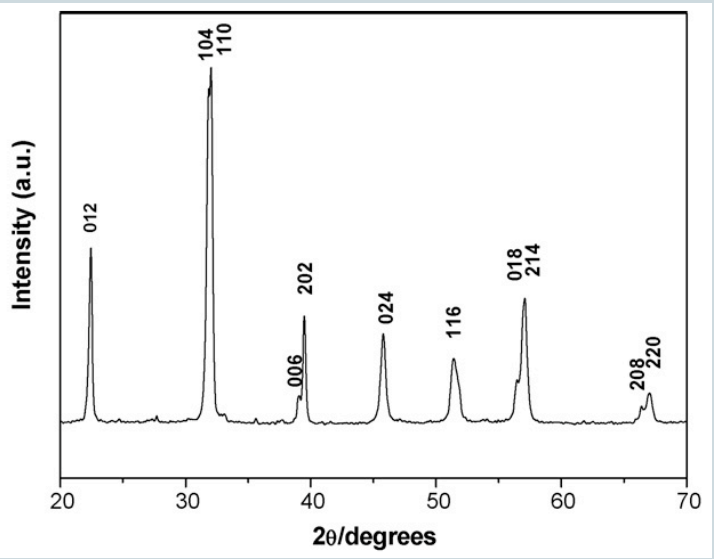

Wang et al. 2009

Multiferróicos – $BiFeO_3$

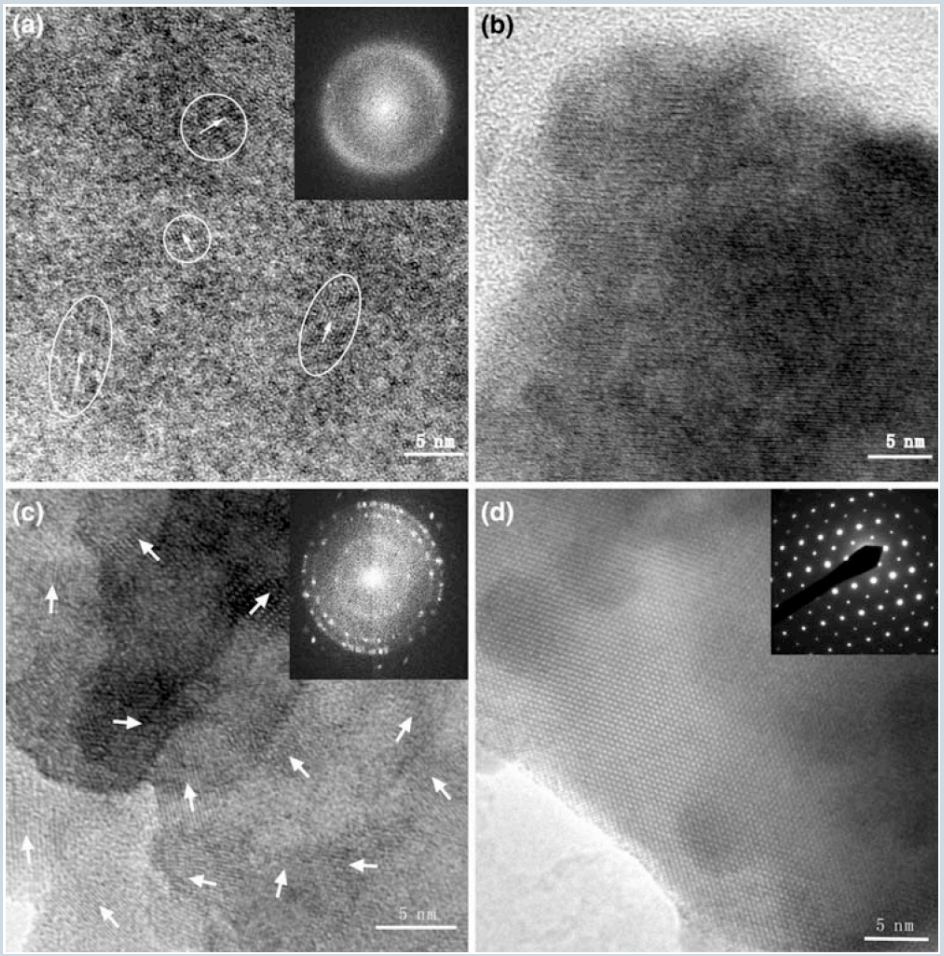

Fig. 3 HRTEM image and the corresponding electron diffraction patterns of (1) (**a**, **b**), (3) (**c**) and (4) (**d**). The *arrows* indicate the direction of crystals

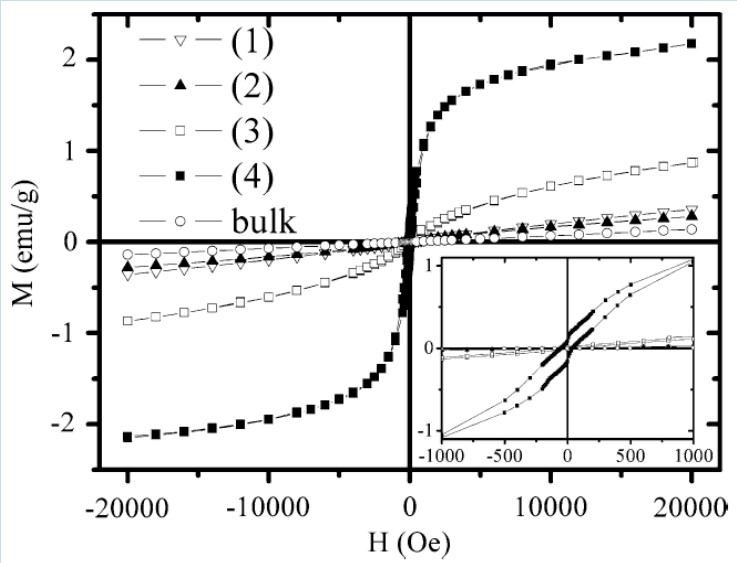

$BiFeO_3$ sintetizado por sol-gel com aquecimento por microondas.

Luo et al. 2009

Multiferróicos – $BiMnO_3$

C2/c

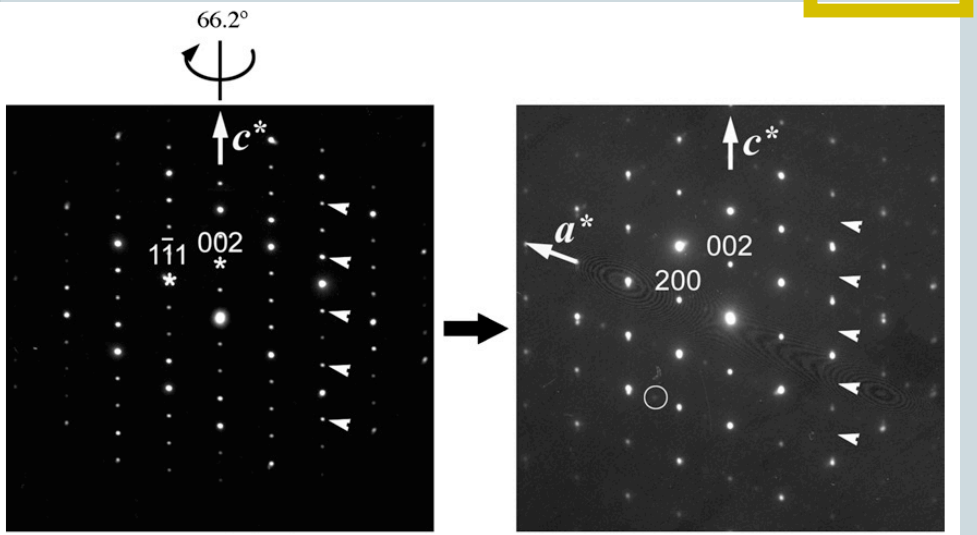

[110] [010]

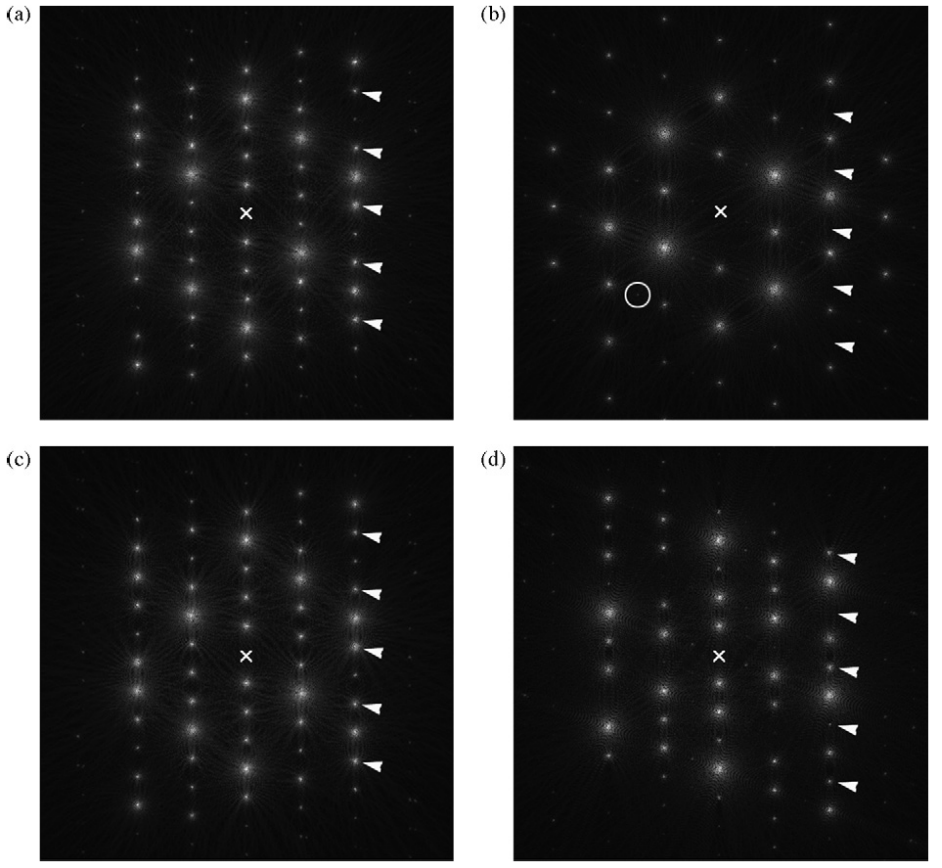

C2

[110] [010]

Yang et al. 2008

Padrão de difração calculado

Multiferróicos – $BiMnO_3$

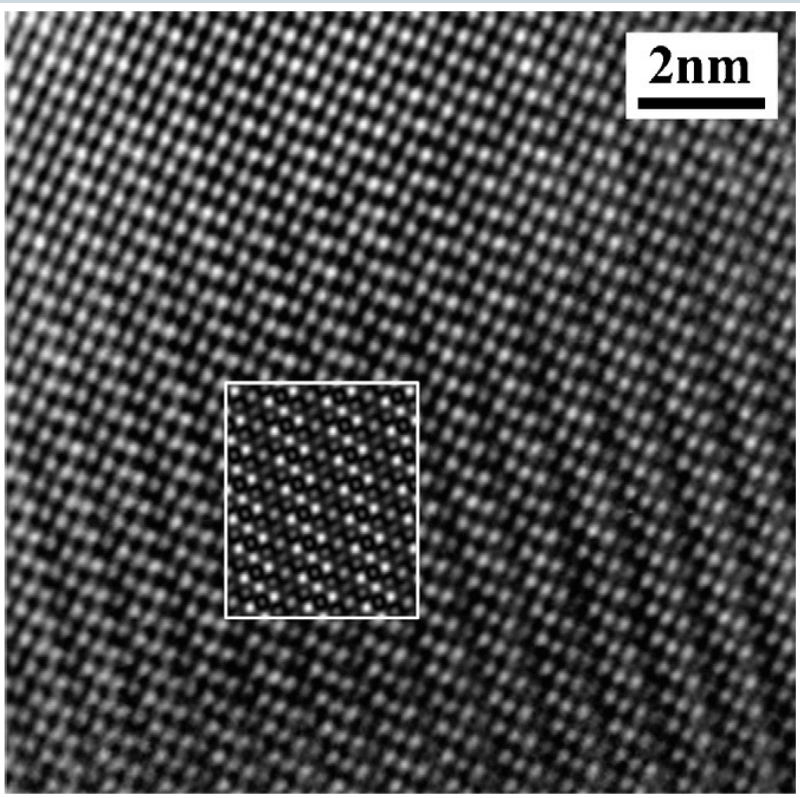

Fig. 5. [1 1 0] HRTEM image taken under the defocus value of approximately −70 nm. A simulated image for a thickness of 15.4 nm and a defocus value of −70 nm is superimposed onto the experimental image to produce the good agreement.

Yang et al. 2008

Epitaxia no Crescimento de $YMnO_3$ sobre Pt e $SrTiO_3$

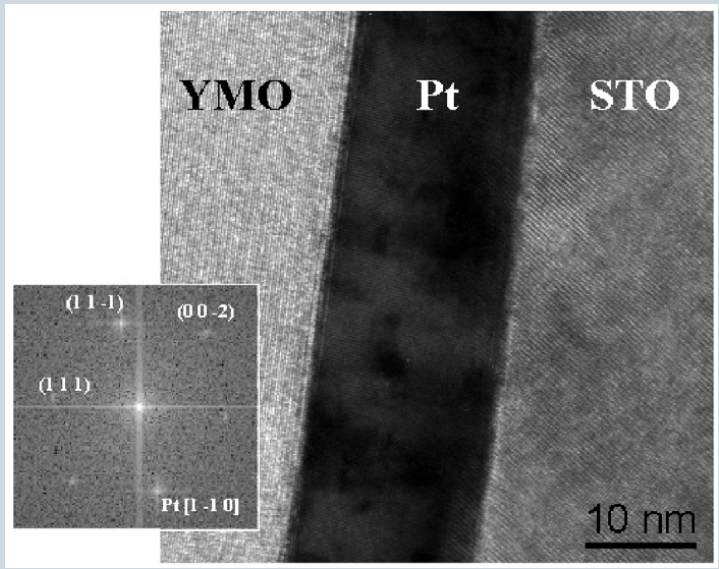

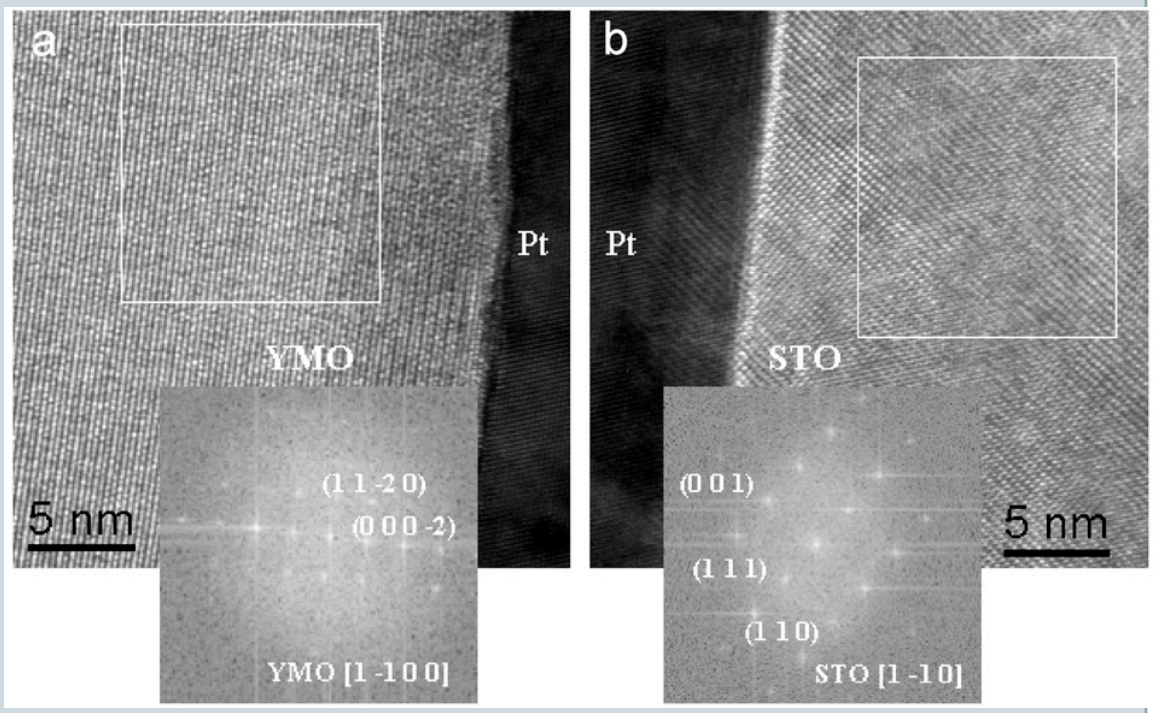

YMO (0001) // Pt (111) // STO (111)

Marti et al. 2007

Revestimento nanocompósito com c-BN e h-BN

Table 1
Lattice plane spacing determined from SAED pattern in Fig. 3 compared with the theoretical values

Latice plane spacing (nm)	Assignment/theoretical value (nm)
0.336	h-Bn (0002)/0.333
0.212	c-BN (111)/0.209
0.182	c-BN (200)/0.181
0.122	c-BN (220)/0.128
0.122	c-BN (311)/0.109
0.092	c-BN (400)/0.090
0.084	c-BN (331)/0.083

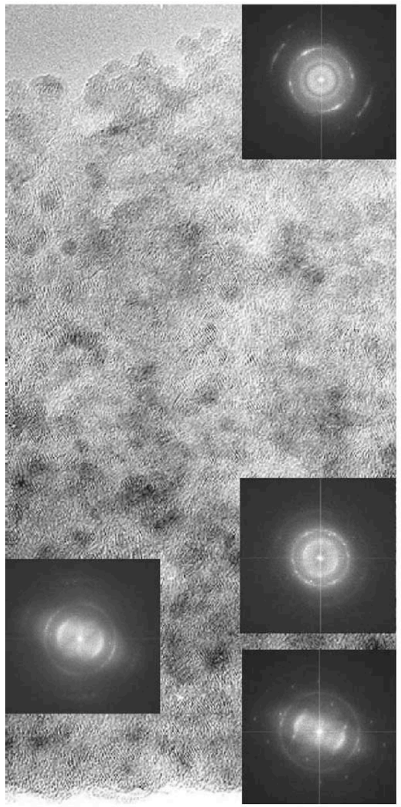

(a) *TEM image of the c-/h-BN film with inserted diffractograms*

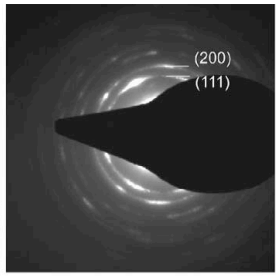

(b) *At the surface*

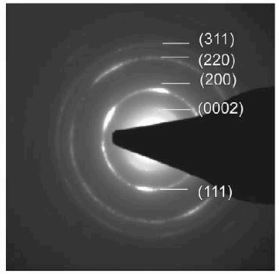

(c) *In the film*

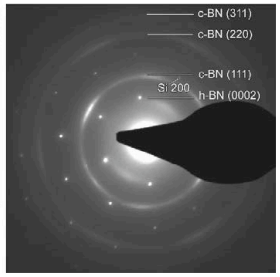

(d) *Interface near region*

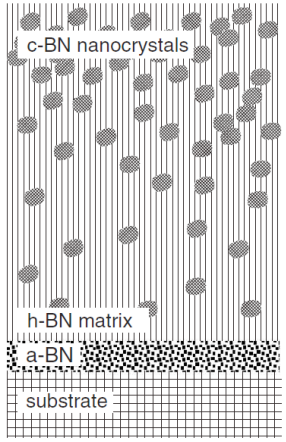

(a) *Schematic of the layered structure*

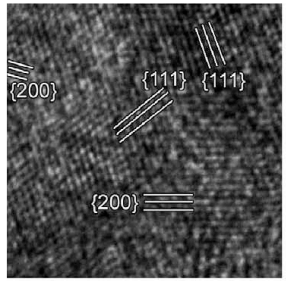

(b) *{111} and {200} planes*

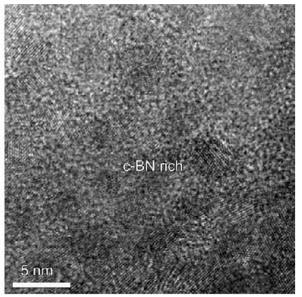

(c) *Surface near region*

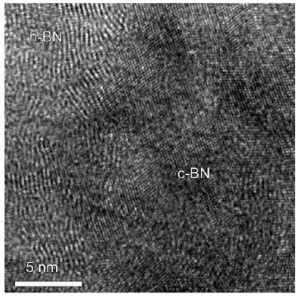

(d) *300 nm above interface*

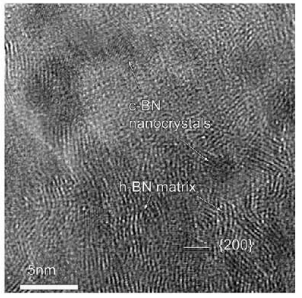

(e) *50 nm above interface*

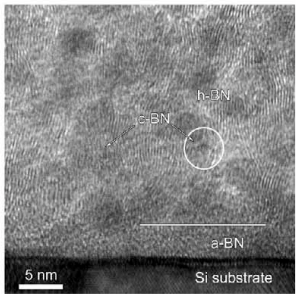

(f) *Interface near region*

Lattemann et al. (2006)

Revestimento de TiN com Cl implantado

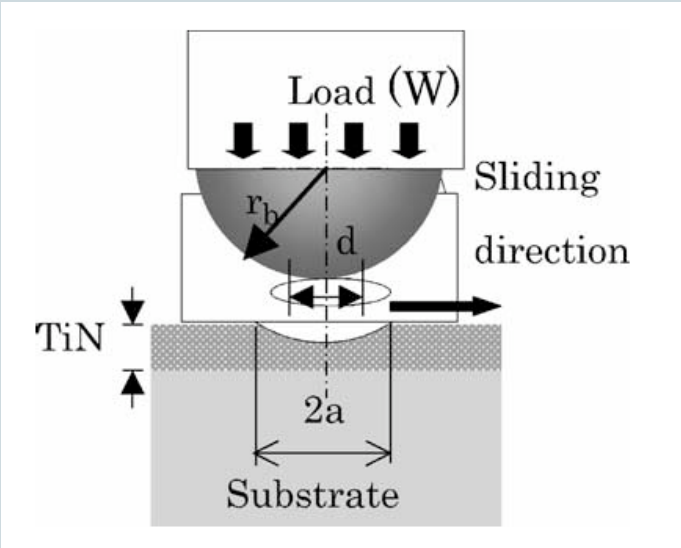

Esfera de Aço INOX 304 (r= 3 mm)
W – 2-5 N
Velocidade – 0,005-0,15 m/s

	As-deposited TiN	Ar-implanted TiN	Cl-implanted TiN
Friction coefficient	0.8–1.2	~1.0	~0.2
Wear coefficient	$\sim 10^{-5}$ to 10^{-4}	$\sim 10^{-4}$	$\sim 10^{-7}$ to 10^{-6}
Wear volume	$\sim 10^{-11}$ m^3	$\sim 10^{-11}$ m^3	$\sim 10^{-13}$ m^3
Wear mode	Adhesive	Adhesive with sticking mode	Abrasive

Akhadejdamrong et al. (2003)

Revestimento de TiN com Cl implantado

$TiO_{1,04}, Ti_7O_{13}, TiO_2$

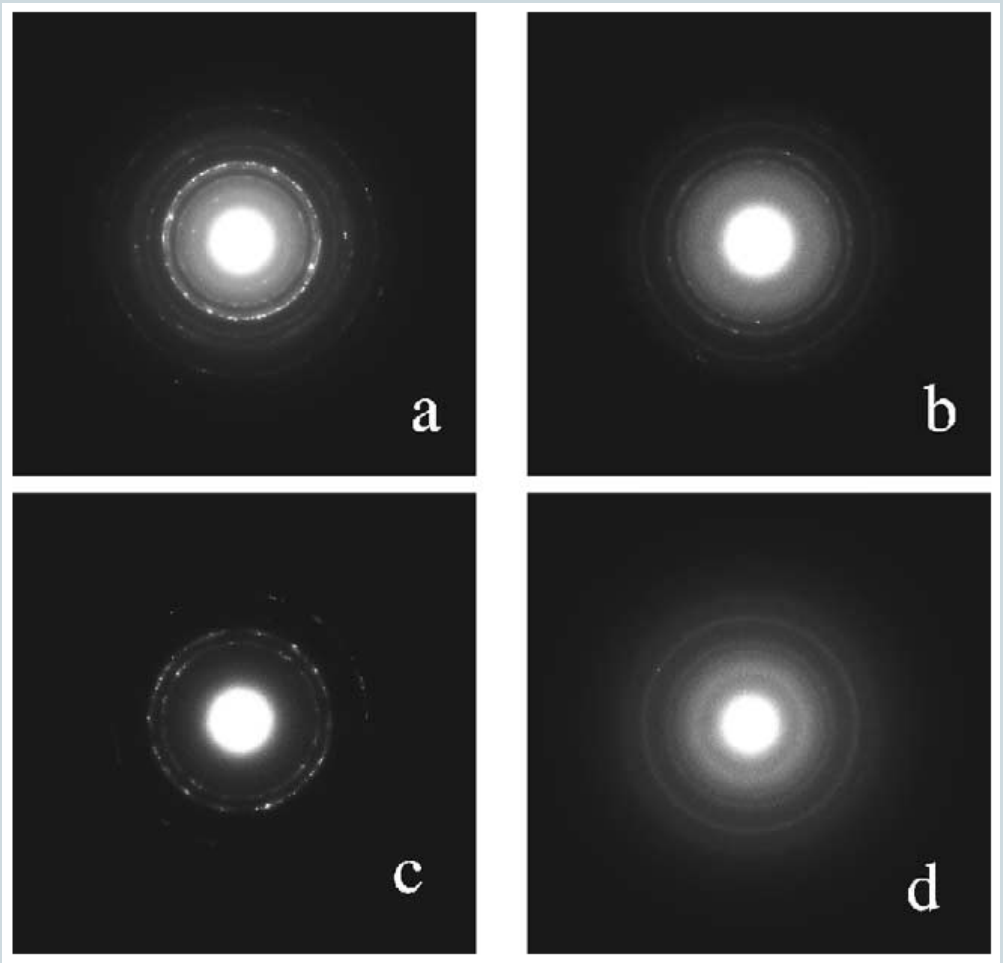

$TiO_{1,04}, Ti_4O_7$

$TiO_{1,04}$

$TiO_{1,04}, Ti_4O_7, Ti_5O_9, TiO_2$

Akhadejdamrong et al. (2003)

Revestimento de TiN com Cl implantado

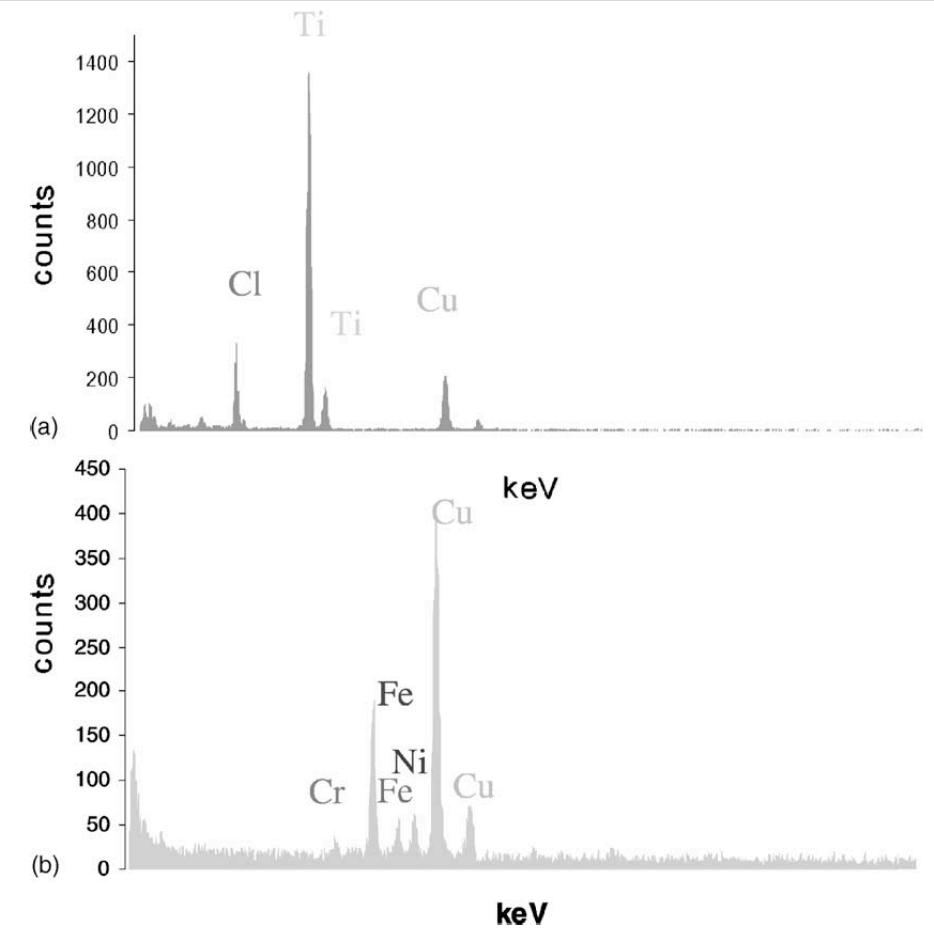

Akhadejdamrong et al. (2003)

Revestimento de TiN com Cl implantado

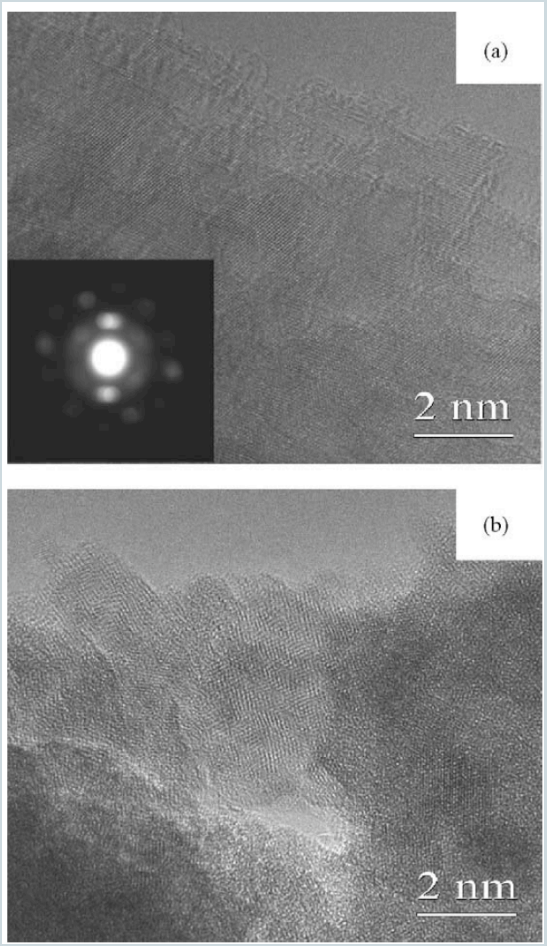

Partícula sem deformação

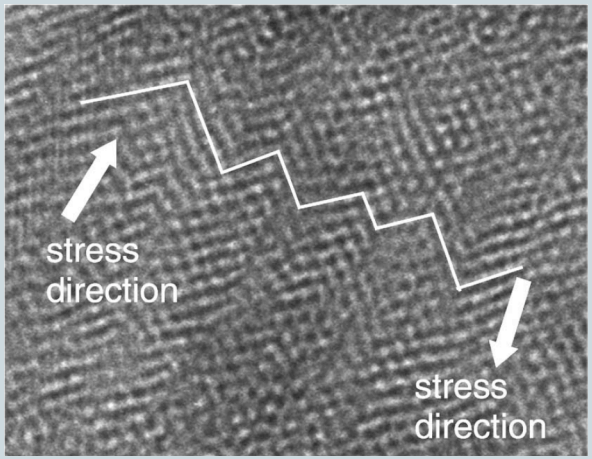

Partícula com padrões de chevron fruto da maclagem para acomodar a deformação cisalhante

Akhadejdamrong et al. (2003)

Revestimento Multicamada de TiAlN/CrN

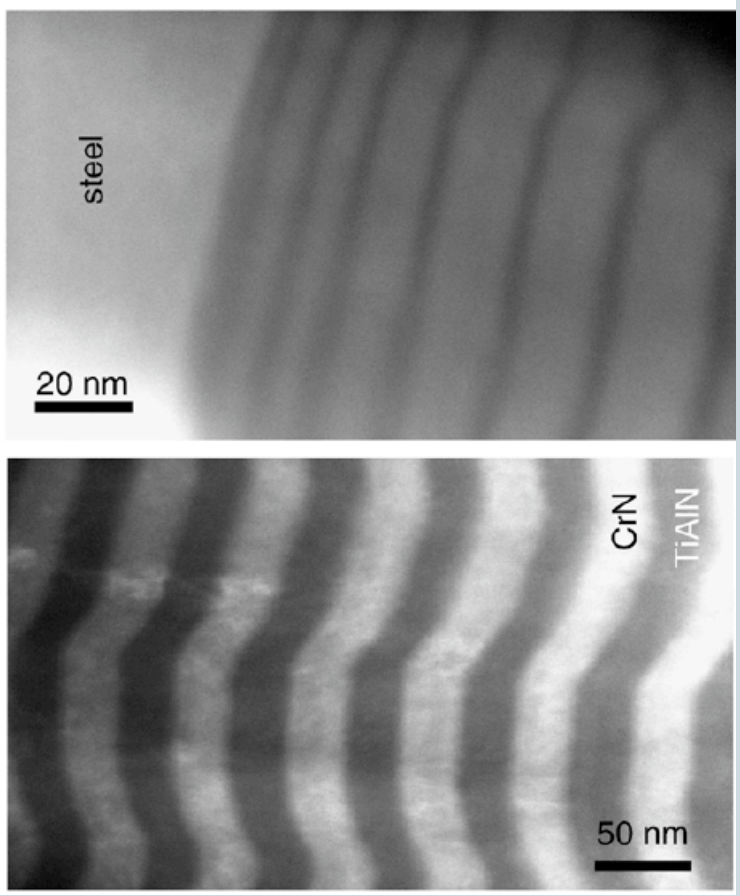

HAADF STEM de camadas de TiAlN/CrN (claro CrN. escuroTiAlN)

Panjan et al. (2007)

Revestimento Multicamada de TiAlN/CrN

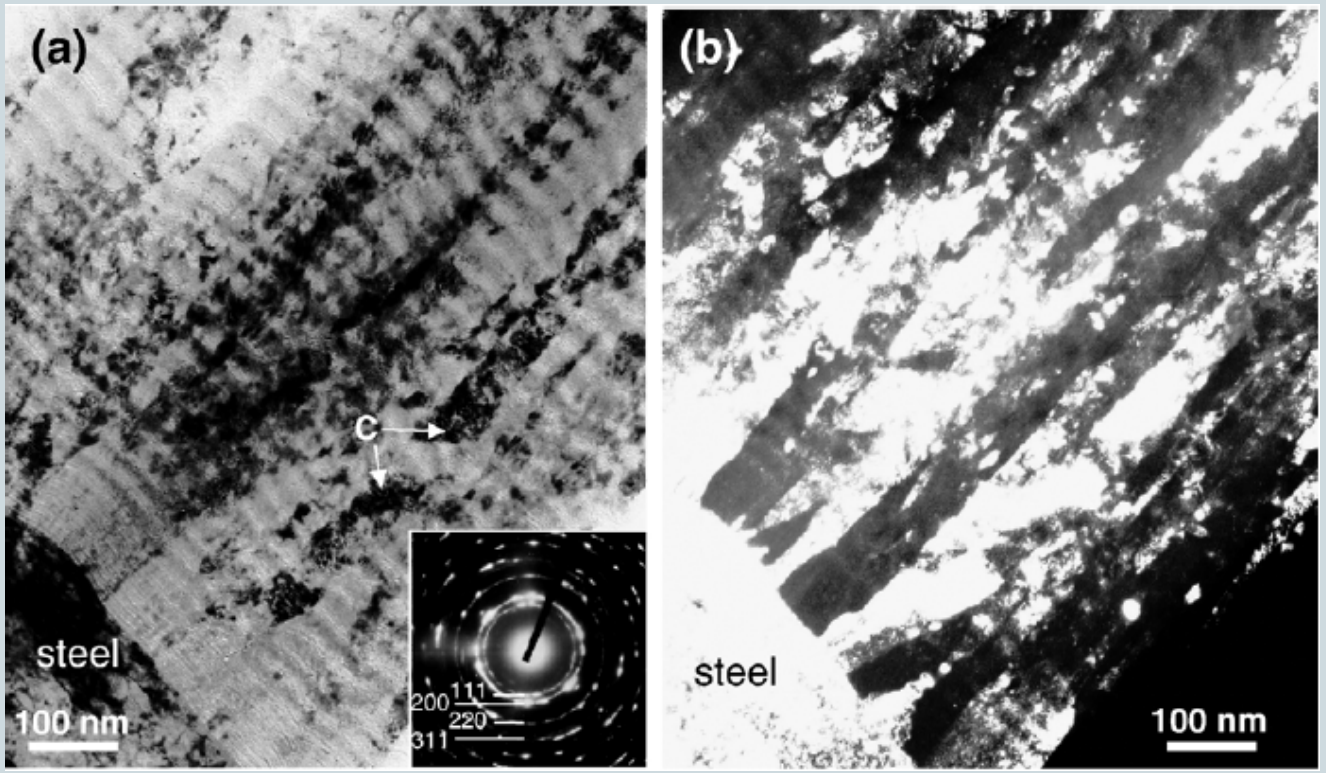

Campo claro Campo escuro

TiAlN/CrN sobre aço depositado por magnetron sputtering reativo

Panjan et al. (2007)

Revestimento Multicamada de TiAlN/CrN

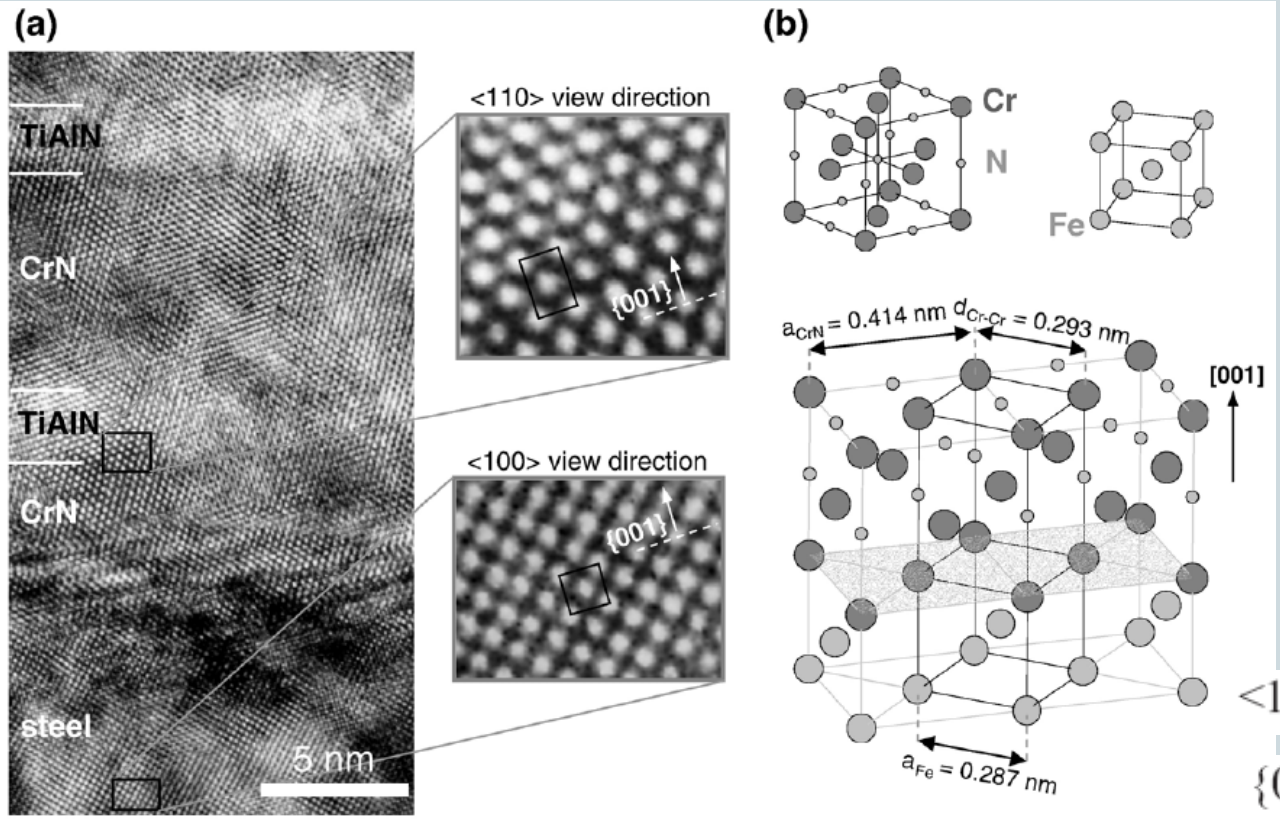

Camadas alternadas de TiAlN e CrN sobre aço. Relação de epitaxia observada

Panjan et al. (2007)

Revestimento Multicamada de TiAlN/CrN

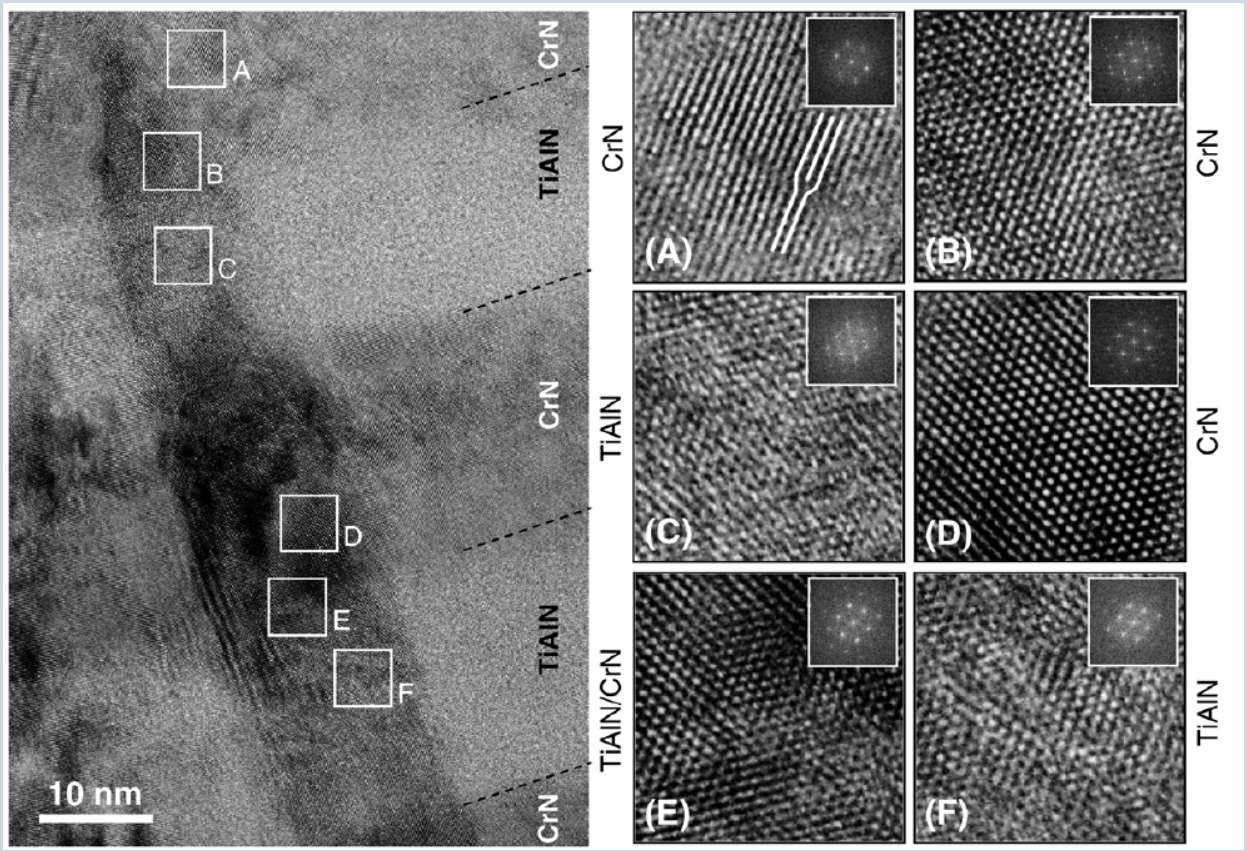

Observação ao longo de um grão colunar, nota-se a epitaxia das camadas ao longo do grão. A-F mostram detalhes em alta resolução, caixas mostram a Transformada de Fourier de cada região.

Panjan et al. (2007)

Liga Ti6Al4V com Revestimento Duplex

Liga base (MO)

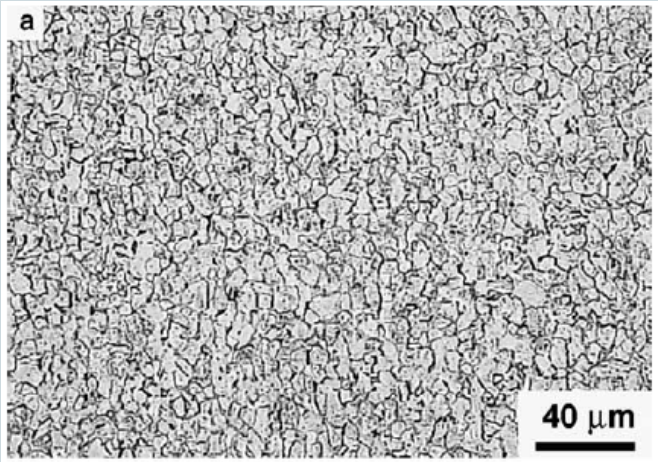

Liga base (TEM)

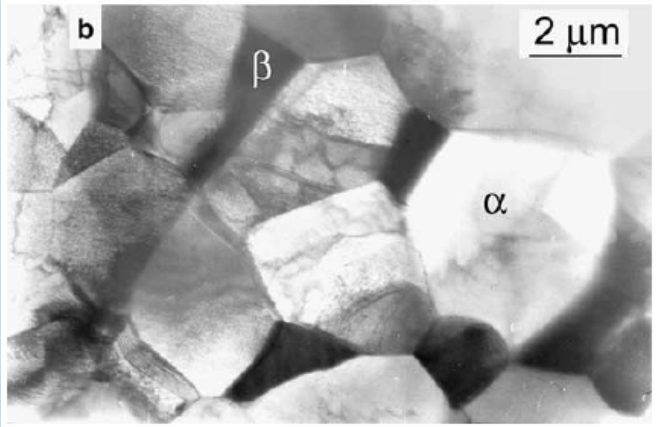

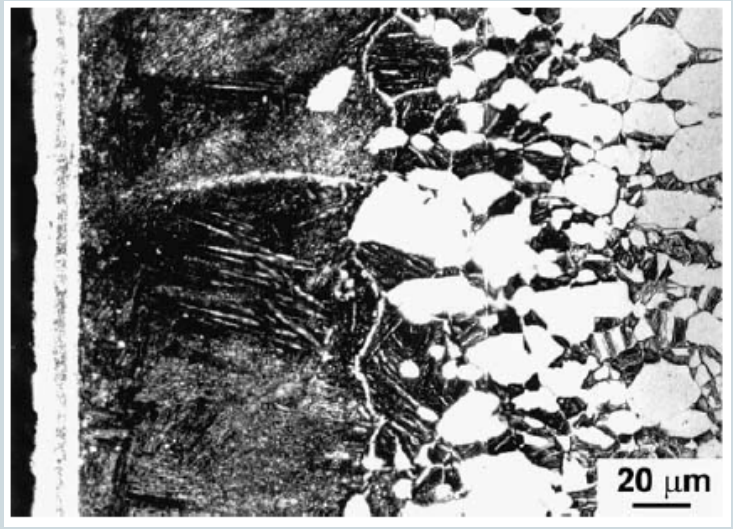

Revestimento (MO)

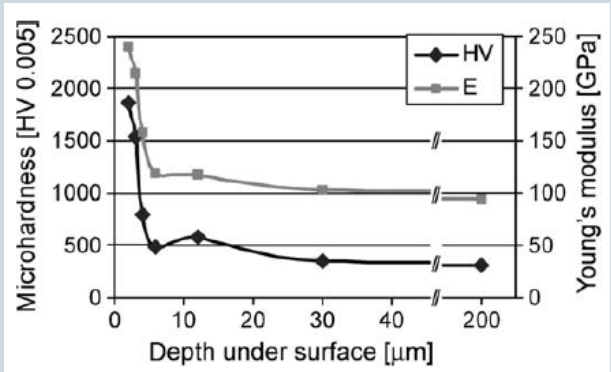

Czyrska-Flemonowicz et al. (2005)

Fluxograma de Identificação

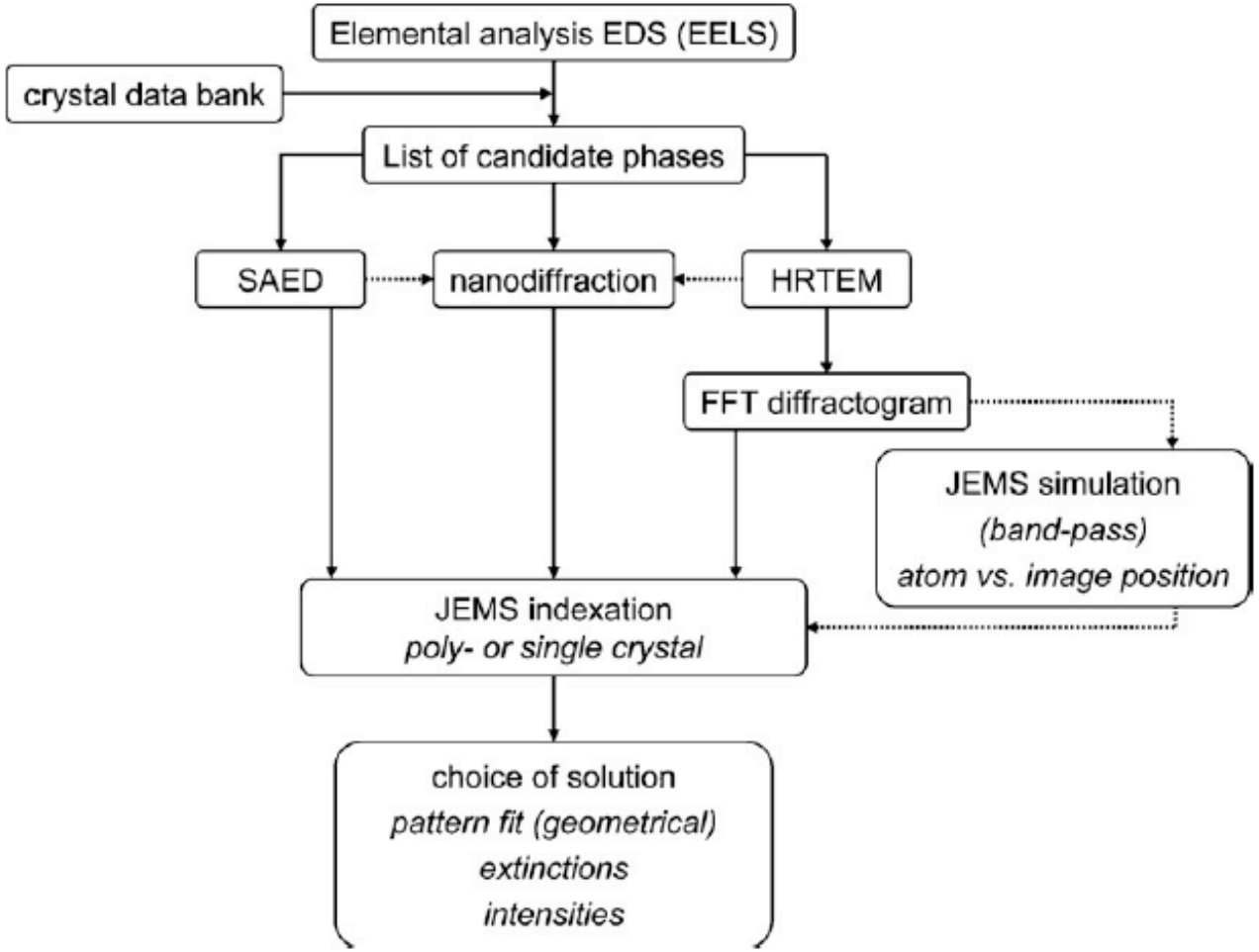

Czyrska-Flemonowicz e Buffat (2009)

Liga Ti6Al4V com Revestimento Duplex

Camadas L5-L1 distintas do revestimento
EDS possibilitou apenas identificar a presença de Ti, Ni, Al, P e O, levando à possibilidade de 27 diferentes fases possíveis

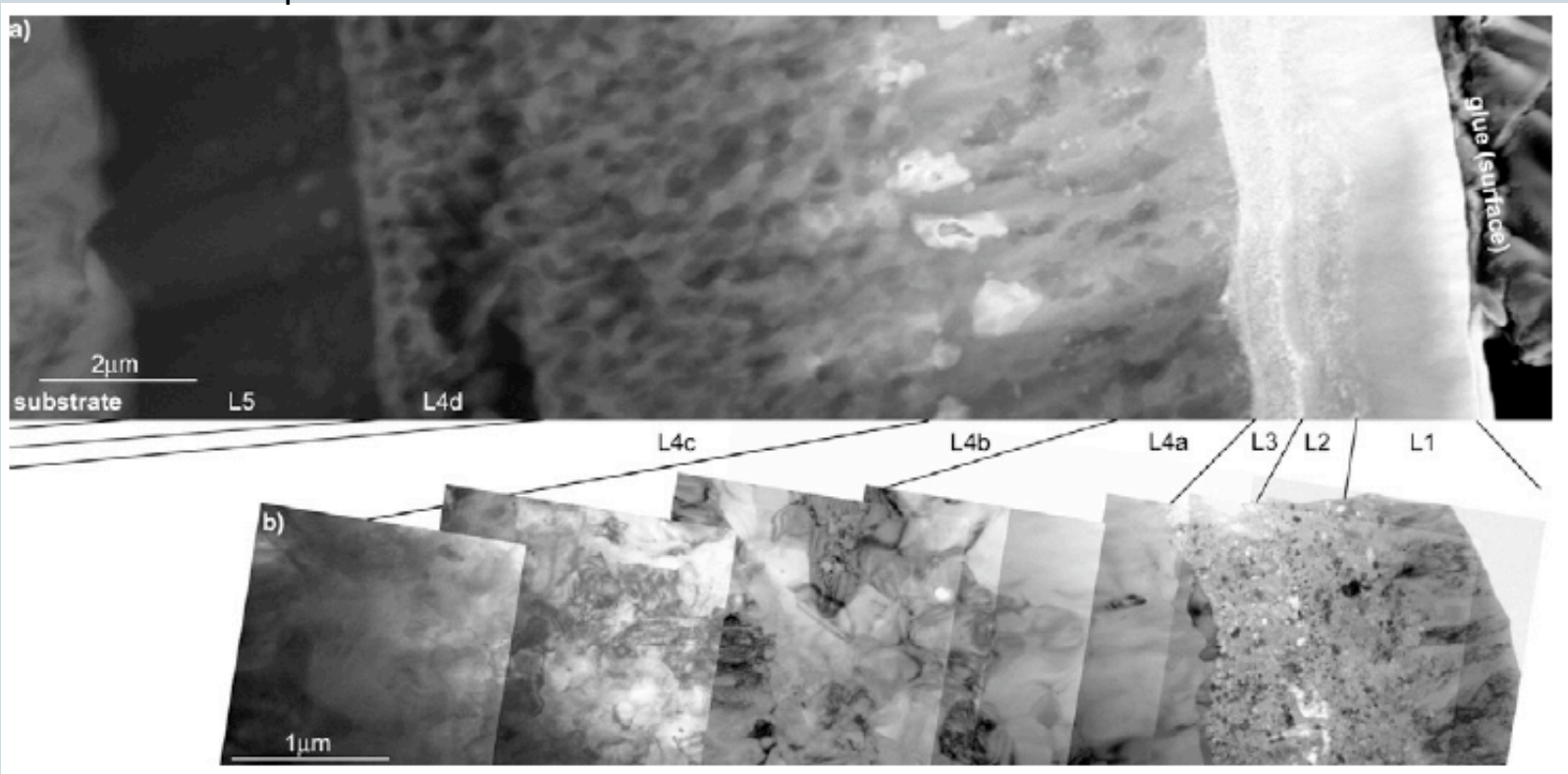

Czyrska-Flemonowicz e Buffat (2009)

Liga Ti6Al4V com Revestimento Duplex

L1 - $NiTi_2$ EDS + SAED

L2 e L3
$NiTi_2$ (linhas cheias) + TiP_3 (meias linhas)

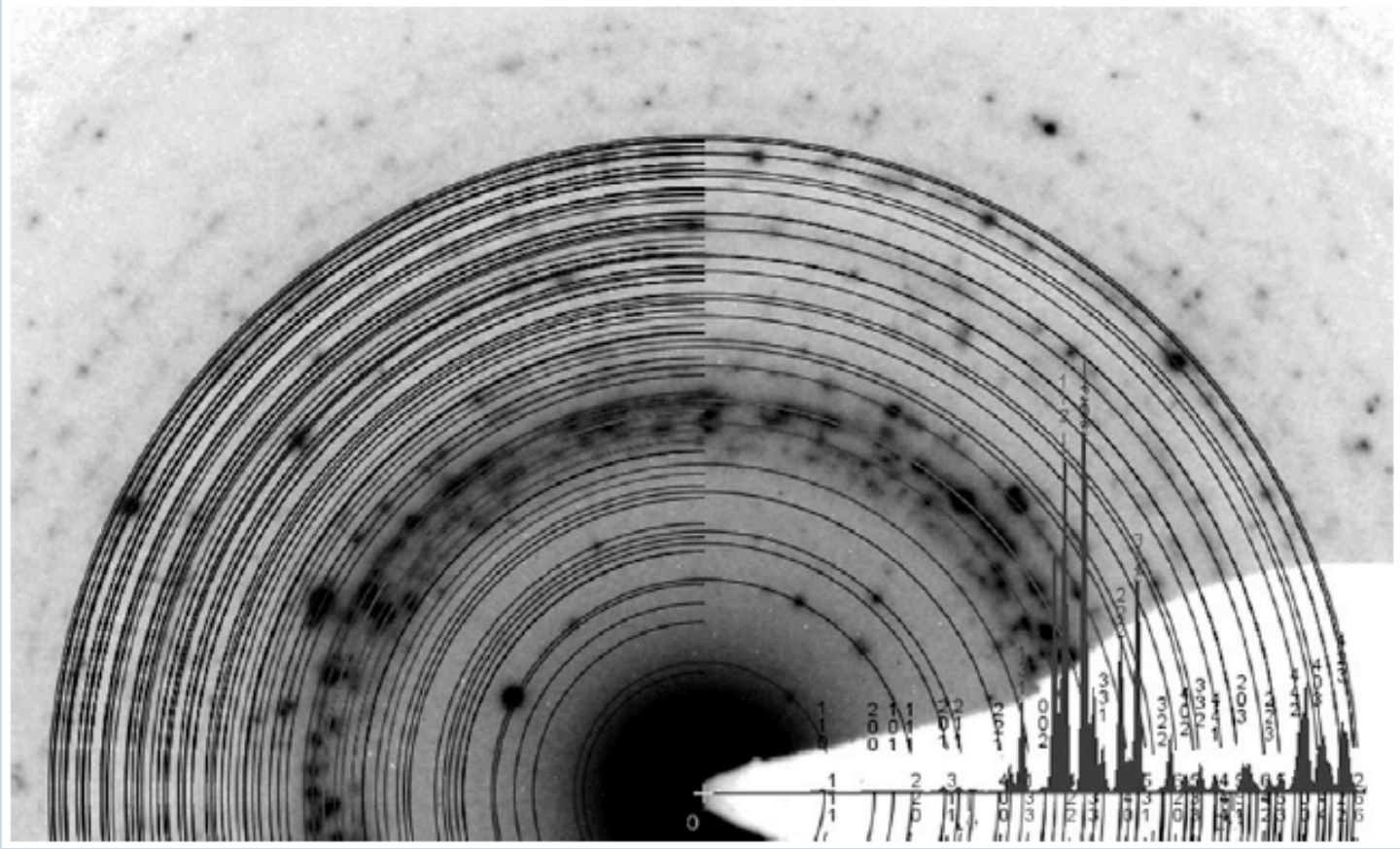

Czyrska-Flemonowicz e Buffat (2009)

Liga Ti6Al4V com Revestimento Duplex

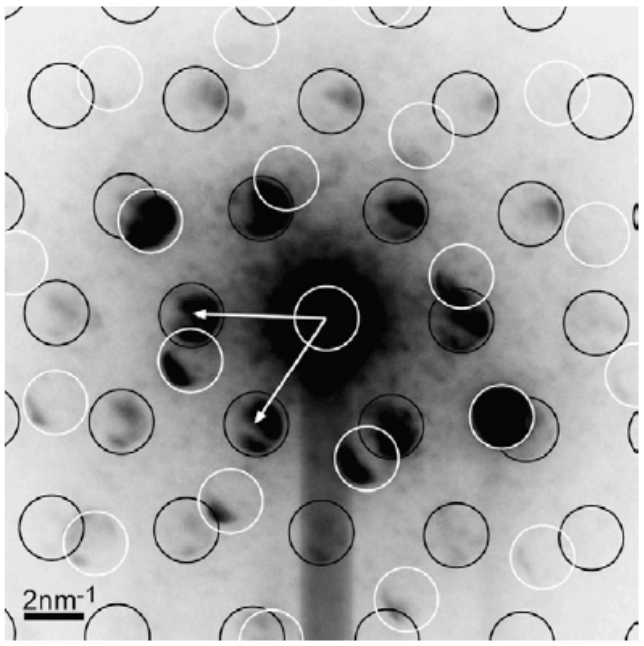

No interior de L2 foi possível observar pequenas fases, cuja identificação indicou para os círculos pretos Ti_2NiP_5 e para os círculos brancos, Ti_2NiP_5,Ti_5P_3 ou TiO.

L1	$NiTi_2$
L2	Major: $NiTi_2$, Ti_3P; minor: TiO; possible: Ti_5P_3, Ti_2NiP_5, $AlNi_2Ti$, N–Ti–(Al)–O
L3	Ni_2Ti, Ti_3P; possible: Ni_3Ti, Ti_5P_3, Ti_2NiP_5
L4/sublayer (a)–(d)	(a) Major: TiNiP; minor: Ni_3Ti, Ti_5P_3; (b) Ni_3Ti, TiNiP, $AlNi_2Ti$; (c) $AlNi_2Ti$; (d) $NiTi_2$, Ti_2P, $AlNi_2Ti$, Ni_5Ti_3Al
L5	Major: $NiTi_2$; isolated precipitates in a sublayer: Ti_3P

Czyrska-Flemonowicz e Buffat (2009)

Liga Ti6Al4V com Revestimento Duplex

Outra possibilidade é obter imagens de alta resolução e construir a Transformada de Fourier, embora seja perdida a informação relativa ao fator de estrutura presente na figura de difração.

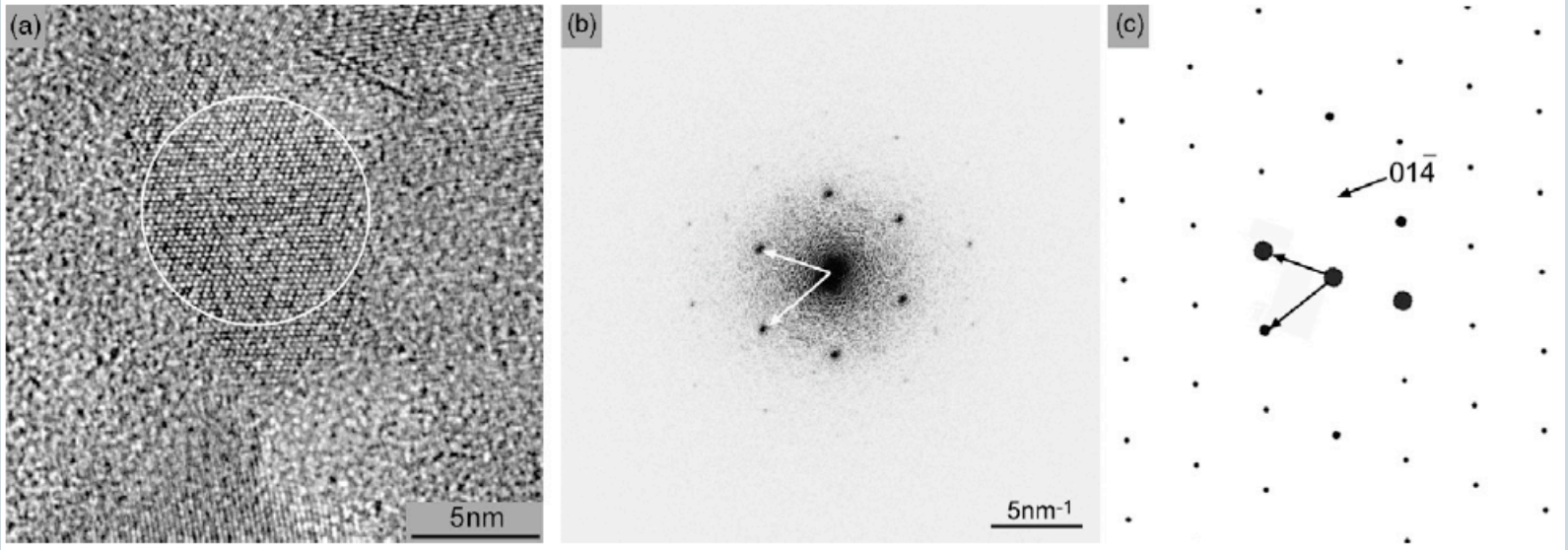

Transformada de Fourier

Padrão de Difração ideal de Ti_2NiP_5

Czyrska-Flemonowicz e Buffat (2009)

Liga Ti6Al4V com Revestimento Duplex

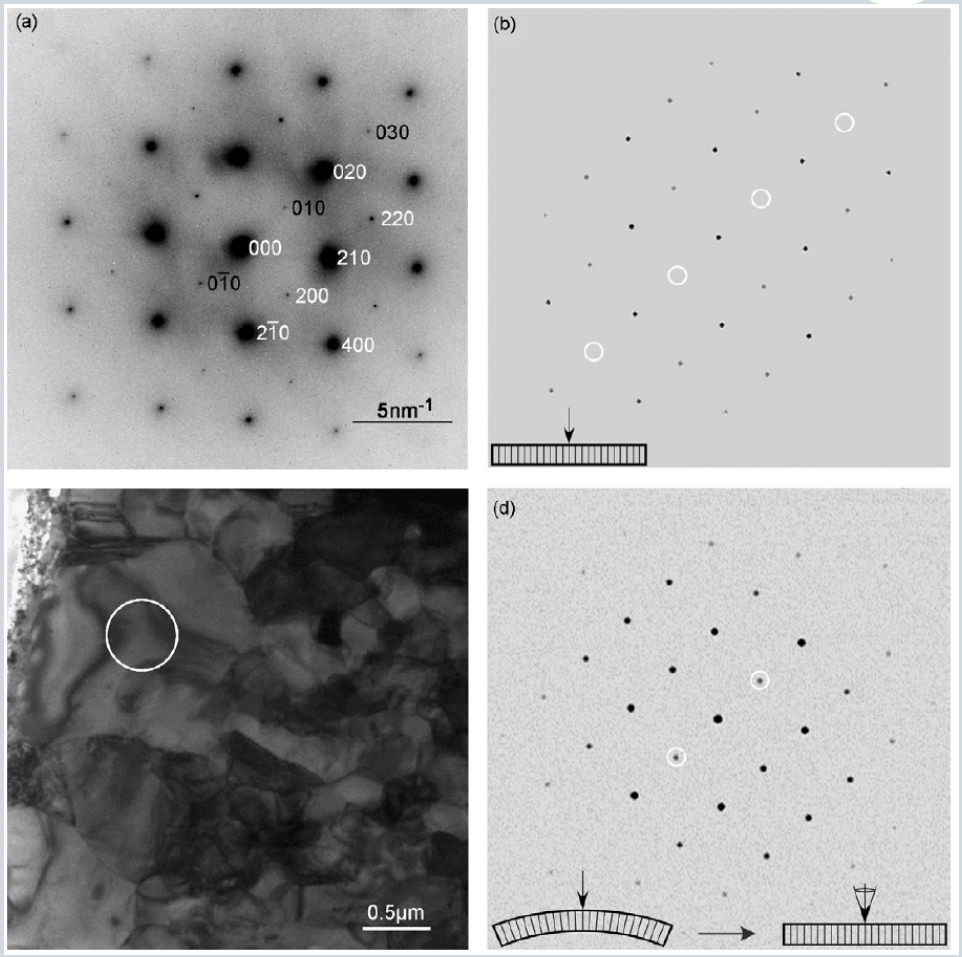

Em L4, a fase preponderante era NiTiP, embora a mesma estivesse deformada, levando à presença de contornos de distorção e da colocação do plano (010) na condição de Bragg

Czyrska-Flemonowicz e Buffat (2009)

Metamateriais a partir de NPs

Table 1. Nanoparticles Used as Building Blocks for BNSLs

NPs	size of crystalline core (nm)	std. %	capping ligand	effective thickness of ligand shell[a] (nm)
Pd	3.0	7		0.85
	3.4	8		
Ag	3.6	7	dodecanethiol	
	4.2	6		
Au	5	7		0.75
	5.8	5		0.9
PbSe	6.2	5	oleic acid	0.85
	7.2	6		
	7.6	5		
$CoPt_3$	6.2	7	ADA, HDA[b]	1
PbS	6.7	5	oleic acid	0.85
γ-Fe_2O_3	13.4	6		0.9

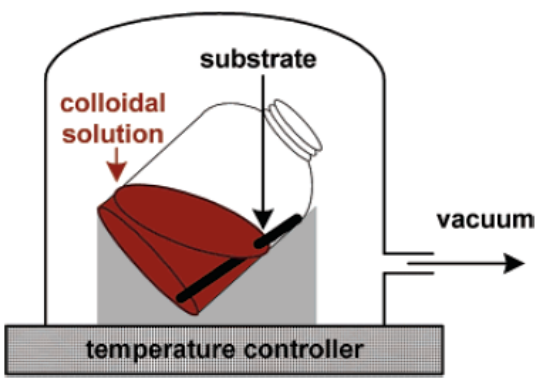

Shevchenko et al. 2006

Table 2. Maximum Packing Density and Range of Stability Calculated for Binary Lattices of Hard Spheres

stoichiometry	type of structure	maximum packing density (γ)	range of stability	ref
AB	NaCl	0.793 (0.414)	below 0.458	27
			$0.2 \le \gamma \le 0.42$	25
	NiAs	0.793 (~0.4)	~0.4	59
	CsCl	0.729, unstable	0.732	60
AB_2	AlB_2	0.778(0.58)	$0.482 \le \gamma \le 0.624$	27
			$0.42 \le \gamma \le 0.59$	25
	Laves phases; hexagonal: $MgZn_2$, $MgNi_2$ cubic $MgCu_2$	0.71 (0.813) unstable	$0.606 \le \gamma \le 0.952$	27
	CaF_2	0.757 unstable	0.225	25
AB_{13}	$NaZn_{13}$ (*ico*-AB_{13})	0.738 (0.58)	$0.54 \le \gamma \le 0.61$	25
			$0.474 \le \gamma \le 0.626$	23,24
	ico-AB_{13}, with some size distribution for B spheres	above 0.755	$0.537 \le \gamma \le 0.583$	27
	cub-AB_{13}	0.700 (0.565)	unstable	27

Metamateriais a partir de NPs

Shevchenko et al. 2006

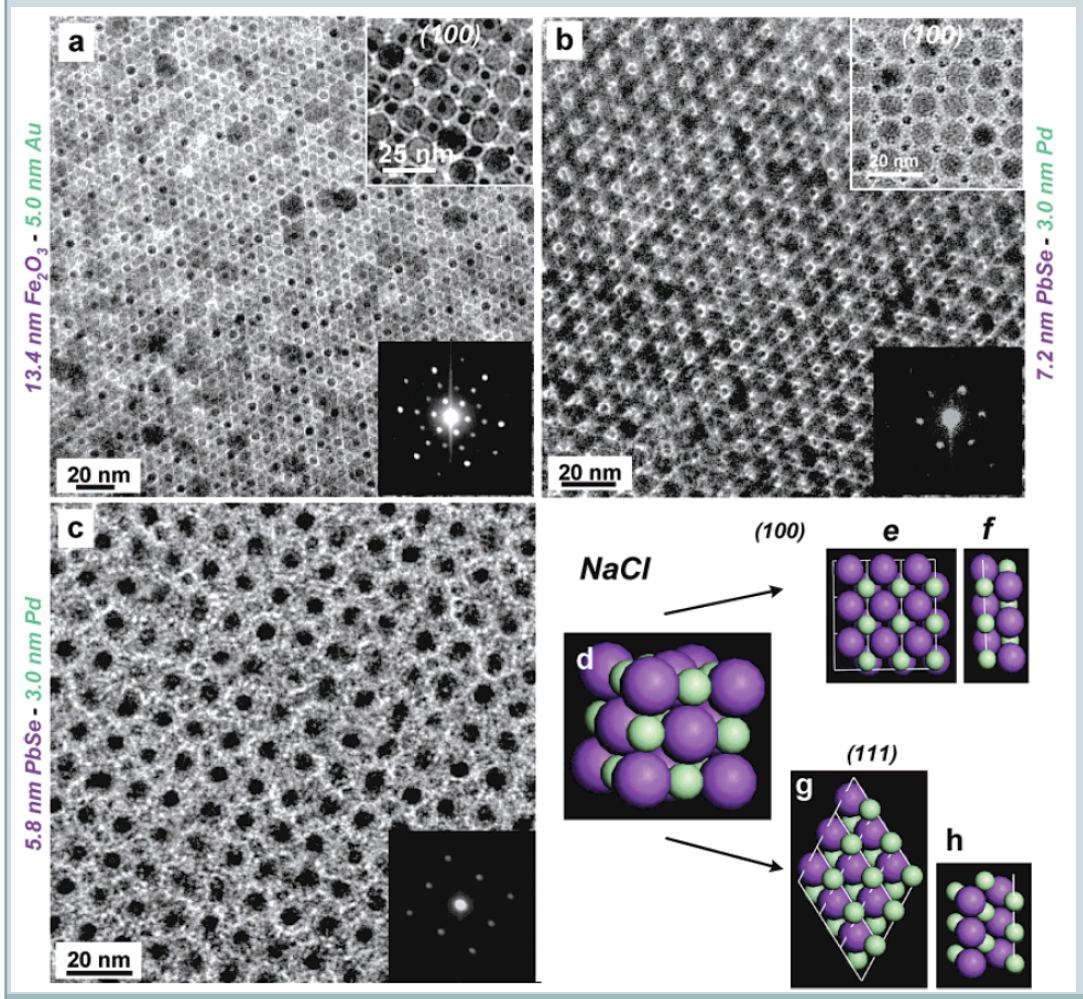

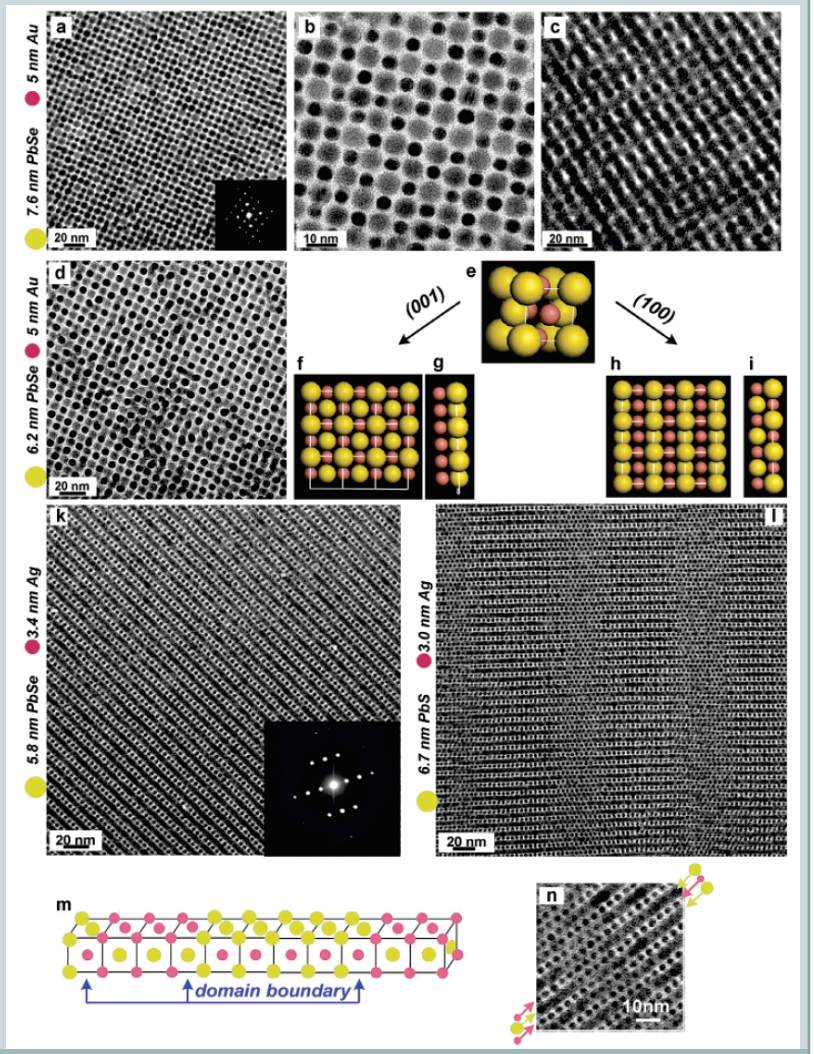

Referências

- Goldstein, J. I. et alli., “Scanning Electron Microscopy and X-Ray Analysis”, Ed. Plenum, New York, 2003.
- Goodhew, P. J. et all, “Electron Microscopy and Analysis”, Ed. Taylor & Francis, London, 2001.
- Lippens, D. “Metamaterials and infra-red applications” C. R. Physique 9 (2008) p. 184-196.
- Wang, Y. “Fabrication and characterization of metallic quase-periodic structures”, Optics Express V16, N2 (2008) p. 1090-1095.
- Lourtioz, J. M. C. R. “New concepts for nanophotonics and nano-electronics – Photonic crystals and metamaterials”, Physique 9 (2008) p. 4-15
- Biener, J. et al. “Nanoporous plasmonic metamaterials”, Advanced Materials 20 (2008) p. 1211-1217.
- Sheridan, A. K. et al. *Fabrication and tuning of nanoscales metallic ring and split-ring arrays*. Journal of Vacuum Science and Technology B 25/6 (2007) p. 2628-263.
- Michael , S. R. et al. *Photonic metamaterials by direct laser writing and silver chemical vapour deposition*. Nature Materials 7 (2008) p. 543-546.
- Thune, E. *Nanostructured sapphire vicinal surfaces as templates for the growth of self-organized oxide nanostructures*. Applied Surface Science 256 (2009) p. 924-928.
- Loesberg et al. Biomaterials V. 28 (2007) p. 3944-3951
- Zhang, M. et al. Science 306, 2004, p. 1358-1361

Referências

- Bastos, A. et al.. Acta Materialia 54 (2006) p. 2451-2462.
- Kelzenberg, M. D. et al.. Nature Materials 9 (2010) p. 239-244
- J. Macêdo. *Formalismo FDTD para a modelagem de meios dispersivos apresentando anisotropia biaxial*. Dissertação. Universidade de São Paulo, 90 p, 2008.
- Pei, Y. T. et al. *Nanostructured TiC/a-C coatings for low friction and wear resistant applications.* Surface & Coatings Technology 198 (2005) p. 44-50.
- Puckett, s. et al. International Journal of Nanomedicine 3 (2008) p. 229-241.

Referências

- Marti, X. et al. “Epitaxial growth of biferroic YMnO3 (0001) on platinum electrodes”, Journal of Crystal Growth 299 (2007) p. 288-294.
- Wang, Y. et al. “Hydrothermal synthesis of single-crystal bismuth ferrite nanoflakes”, Ceramics International 35 (2009) p. 1285-1287.
- Czyrska-Flemonowicz, A. E Buffat, P. A. *Characterization of phases in nanostructured, multilayered titanium alloys by analytical and high-resolution electron microscopy*. Micron 40 (2009) p. 15-21.
- Czyrska-Flemonowicz, A. , E Buffat, P. A. e Wierzchon, T. *Microstructure and properties of hard layers formed by duplex surface treatment containing nickel and phosphorous on a titanium-base alloy*. Scripta Materialia 53 (2005) p. 1439-1442.
- Sung, S. L. et al.. *The strenghtening mchanisms of DLC film on silicon by MPECVD.* Thin Solid Films 315 (1998) p. 345-350.
- Choi, W. S e Hong B.. *The effect of annealing on the properties of diamond-like carbon protectie antireflection coatings.* Renewable Energy 33 (2008) p. 226-231.
- Akhadejdamrong, T. et al. *Self-lubricatin mechanism of chlorine implanted TiN coatings.* Wear 254 (2003) p. 668-679.
- Thune, E. *Nanostructured sapphire vicinal surfaces as templates for the growth of self-organized oxide nanostructures*. Applied Surface Science 256 (2009) p. 924-928.

Referências

- Qin, F. X. et al. *Microstructure and electrochemical behavior of Ti-coated $Zr_{55}Al1_0Ni_5Cu3_0$ bulk metallic glass*. Intermetallics 17 (2009) p. 945-950.
- Kovalev, A. I. et al. *Impact of Al and |Cr alloying in TiN-based PVD coatings on cutting performance during machining of hard to cut materials*. Vacuum 84 (2010) p. 184-187.
- Mesanta, M et al. *Development of a hard nano-structured multi-component ceramic coating by laser cladding.* Materials Science and Engineering A 508 (2009) p. 134-140.
- Fernandes, C. et al. *Effect of the microstructure on the cutting performance of superhard (Ti, Si, Al)N nanocomposite films*. Vacuum 82 (2008) p. 1470-1474.
- Latteman et al. *Stress reduction in nanocomposite coatings consisting of hexagonal and cubic boron nitride*. Surface & Coatings Technology 200 (2006) p. 6459-6464.
- Sheridan, A. K. et al. *Fabrication and tuning of nanoscales metallic ring and split-ring arrays*. Journal of Vacuum Science and Technology B 25/6 (2007) p. 2628-263.
- Michael , S. R. et al. *Photonic metamaterials by direct laser writing and silver chemical vapour deposition*. Nature Materials 7 (2008) p. 543-546.
- Shevchenko, E. V. et al. Characterization of Self-Assembled Multifunctional Binary nanoparticles Superlattices, J. Am. Chem. Soc. 128 (2006) p. 3620-3637.

- Obrigado pela atenção

André L. Pinto

pinto@cbpf.br